UPPSALA
UNIVERSITET

Digital Comprehensive Summaries of Uppsala Dissertations from the Faculty of Science and Technology 1018

Electronic Sensors Based on Nanostructured Field-Effect Devices

SI CHEN

ACTA
UNIVERSITATIS
UPSALIENSIS
UPPSALA
2013

ISSN 1651-6214
ISBN 978-91-554-8596-2
urn:nbn:se:uu:diva-194015

Dissertation presented at Uppsala University to be publicly examined in Häggsalen, Ångström Laboratory, Lägerhyddsvägen 1, Uppsala, Wednesday, March 27, 2013 at 10:00 for the degree of Doctor of Philosophy. The examination will be conducted in English.

Abstract
Chen, S. 2013. Electronic Sensors Based on Nanostructured Field-Effect Devices. Acta Universitatis Upsaliensis. *Digital Comprehensive Summaries of Uppsala Dissertations from the Faculty of Science and Technology* 1018. 71 pp. Uppsala. ISBN 978-91-554-8596-2.

Point-of-care (POC) diagnostics presents a giant market opportunity with profound societal impact. In particular, specific detection of DNA and protein markers can be essential for early diagnosis of *e.g.* cancer, cardiovascular disease, infections or allergies. Today, identification of these markers often requires extensive laboratory work and hence is expensive and time consuming. Current methods for recognition and detection of specific biomolecules are mostly optics based and thus impose severe limitations as to convenience, specificity, sensitivity, parallel processing and cost reduction.

Electronic sensors based on silicon nanowire field-effect transistors have been reported to be able to detect biomolecules with concentrations down to femtomolar (fM) level with high specificity. Although the reported capability needs further confirmation, the CMOS-compatible fabrication process of such sensors allows for low cost production and high density integration, which are favorable for POC applications. This thesis mainly focuses on the development of a multiplex detection platform based on silicon nanowire field-effect sensors integrated with a microfluidic system for liquid sample delivery. Extensive work was dedicated to developing a top-down fabrication process of the sensors as well as an effective passivation scheme. The operation mechanism and coupling efficiencies of different gate configurations were studied experimentally with the assistance of numerical simulation and equivalent circuits. Using *p*H sensing as a model system, large effort was devoted to identifying sources for false responses resulting from the instability of the inert-metal gate electrode. In addition, the drift mechanism of the sensor operating in electrolyte was addressed and a calibration model was proposed. Furthermore, protein detection experiments were performed using small-sized Affibody molecules as receptors on the gate insulator to tackle the Debye screening issue. Preliminary results showed that the directionality of the current changes in the sensors was in good agreement with the charge polarities of the proteins. Finally, a graphene-based capacitor was examined as an alternative to the nanowire device for field-effect ion sensing. Our initial attempts showed some attractive features of the capacitor sensor.

Keywords: biosensor, field-effect transistor, nanowire, ISFET

Si Chen, Uppsala University, Department of Engineering Sciences, Solid State Electronics, Box 534, SE-751 21 Uppsala, Sweden.

ISSN 1651-6214
ISBN 978-91-554-8596-2
urn:nbn:se:uu:diva-194015 (http://urn.kb.se/resolve?urn=urn:nbn:se:uu:diva-194015)

List of Appended Papers

This thesis is based on the following papers, which are referred to in the text by their Roman numerals.

I Chen S., Zhang S.-L. (2011) Gate coupling and carrier distribution in silicon nanowire/nanoribbon transistors operated in electrolyte, *Journal of Vacuum Science & Technology A*, 29(1): 011022

II Chen S., Zhang S.-L. (2011) Contacting versus insulated electrodes in silicon nanoribbon field-effect sensors operating in electrolyte, *Analytical Chemistry*, 83 (24): 9546–9551

III Chen S., Nyholm L., Jokilaakso N., Karlström A. E., Linnros J., Smith U., Zhang S.-L. (2011) Current instability for silicon nanowire field-effect sensors operating in electrolyte with platinum as gate electrode, *Electrochemical and Solid-State Letters*, 14(7): J34-J37

IV Chen S., Jokilaakso N., Björk P., Eriksson Karlström A., Zhang S.-L. (2010) A two-terminal silicon nanoribbon field-effect pH sensor, *Applied Physics Letters*, 97(26): 264102

V Chen S., Zhang Z.-B., Ma L., Ahlberg P., Gao X., Qiu Z., Wu D., Ren W., Cheng H.-M., Zhang S.-L. (2012) A graphene field-effect capacitor sensor in electrolyte, *Applied Physics Letters*, 101(15):154106

Acknowledgements

I'm profoundly grateful to my supervisor, Professor Shi-Li Zhang for bringing me into this exciting and challenging research field. During my PhD period, I have received enormous help, encouragement and patient guidance from him. His rigorous and optimistic attitude towards scientific research will be beneficial for my future career. I also would like to express my gratitude to my co-supervisor Professor Jan Linnros. I had really nice time during my stay with his group and would like to thank him for his help and support during my work in his lab.

Deep gratitude is given to my practical supervisor in KTH, Dr. Yong-Bin Wang for teaching me silicon processes in the cleanroom and software for design and simulation.

I'm very grateful to all group members at Emerging Electronics at the Laboratory of Solid-State Electronics, Dr. Zhibin Zhang, Malkolm Hinnemo, Dr. Zhiwei Zhu, Dr. Xindong Gao, Zhiying Liu, Patrik Ahlberg, Balazs Farkas, Da Zhang, Man Song, Seung Hee Jeong and Seyed Reza Moossavi for their kind help, support and fruitful discussions.

I would like to thank all biosensor project members, Nima Jokilaakso, Viktor Tullgren, Andréas Larsson, Per Björk, Tommy Schönberg, Roodabeh Afrasiabi, Jan Linnros (again), Amelie Eriksson Karlström, Christian Vieider, Christian Valenzuela Köhnenkamp, for their interest, advices and support to my work.

Many thanks are given to my colleagues at KTH and Uppsala University for their kind help, support and fruitful discussions. They are Docent Per-Erik Hellström, Professor Anders Hallén, Dr. Gunnar Malm, Christian Ridder, Timo Söderqvist, Dr. Jiantong Li, Ling-Guang Li, Docent Hans Norström, Dr. Klas-Håkan Eklund, Professor Ulf Smith, Professor Jörgen Olsson, Dr. Örjan Vallin, Dr. Lars Vestling, Kristina Wiberg and Dr. Uwe Zimmermann.

I'm very grateful to Professor Leif Nyholm for helping me understand the electrochemical problems and to Professor Ulf Landegren for fruitful discussions on biological processes.

My deep gratitude is also directed to Professor Jörgen Olsson (again) and Dr. Jonathan Scragg for taking your precious time to screen the thesis and to give me concrete and useful comments and suggestions for improvement.

Many thanks go to Marianne Asplund for all your administrative help.

The staff at Electrum laboratory and Ångström laboratory is acknowledged for their work to keep the lab running smoothly.

Finally, I would like to thank my parents, sister, wife and son for all your love and support during all these years.

Si Chen

Feb. 2013 Uppsala

Table of Contents

List of Symbols & Acronyms

b_m	Surface concentration of receptors on the sensor
C_D	Depletion capacitance
C_d	Differential capacitance
C_{BG}	Back gate capacitance
C_{TG}	Top gate capacitance
C_G	Gate capacitance
C_{ox}	Oxide capacitance
C_{sub}	Substrate capacitance
C_q	Quantum capacitance
D	Diffusivity
Da	Damkohler number
E_{ME}	Electrode potential
F	Faraday constant
G	Conductance
I_{DS}	Drain-to-source current
I_{DSsat}	Drain-to-source saturation current
$I_{on}(I_{off})$	On(off) current
J_D	Biomolecule flux to sensor surface
k	Boltzmann's constant
K	Reaction equilibrium constant
$k_{on}(k_{off})$	Association(dissociation) constant
n^0	Number concentration of ions in a z:z electrolyte
N_A	Acceptor-impurity concentration
N_D	Donor-impurity concentration
N_S	Number of surface sites
P	Ionic strength of electrolyte
Pe	Peclet number
$p\mathrm{H}_B$	pH level in bulk electrolyte
$p\mathrm{H}_{pzc}$	Point of zero charge
$p\mathrm{H}_S$	pH level at surface
q	Electronic charge (1.6×10^{-19} C)
Q_f	Fixed oxide charge density
Q_m	Mobile ionic charge density
Q_{ot}	Oxide trapped charge density
SS	Subthreshold slope
t	Time

T	Kelvin temperature
V_D	Drain voltage
V_{Dsat}	Drain saturation voltage
V_G	Gate voltage
V_{TH}	Threshold voltage
z	Charge magnitude of ions in a z:z electrolyte
α	Dimensionless sensitivity parameter of gate insulator
β_{int}	Intrinsic buffer capacity
δ_s	Thickness of depletion zone in fluid
ε_{Si}	Relative permittivity of silicon
κ^{-1}	Debye length
μ_j	Chemical potential of species j
$\overline{\mu_i}$	Electrochemical potential of species j
μ_n	Electron mobility
μ_p	Hole mobility
σ_s	Surface charge density
φ_d	Donnan potential
φ_{ME}	Potential drop over metal/electrolyte interface
φ_s	Surface potential at insulator/electrolyte interface
Φ_m	Metal work function
Φ_{Si}	Silicon work function
χ^{sol}	Surface dipole potential of solvent
ψ_B	Potential difference between Fermi and intrinsic level
ψ_{EL}	Electrical potential in electrolyte
AFM	Atomic force microscopy
APDMS	(3-Aminopropyl)dimethylethoxysilane
APTES	(3-Aminopropyl)triethoxysilane
BOX	Buried oxide
CAM	Contact angle measurement
DOS	Density of states
dsDNA	Double-stranded DNA
EDC	Ethyl(dimethylaminopropyl) carbodiimide
EDL	Electrical double layer
GCS	Gouy-Chapman-Stern
HSA	Human serum albumin
IHP	Inner Helmholtz plane
ISFET	Ion selective field-effect transistor
LOCOS	Local oxidation of silicon
MOSFET	Metal-oxide-semiconductor field-effect transistor
NHS	*N*-hydroxysuccinimide
NW	Nanowire
OHP	Outer Helmholtz plane
*p*I	Isoelectric point
PBS	Phosphate buffered saline

PDMS	Polydimethylsiloxane
PECVD	Plasma-enhanced chemical vapor deposition
POC	Point of care
PSA	Prostate-specific antigen
QCM	Quartz crystal microbalance
redox	Reduction-oxidation
RTO	Rapid thermal oxidation
SAM	Self-assembled monolayer
SiNWFET	Silicon nanowire field-effect transistor
SOI	Silicon-on-insulator
SPR	Surface plasmon resonance
ssDNA	Single-stranded DNA
TMAH	Tetramethylammonium hydroxide
VLS	Vapor-liquid-solid
XPS	X-ray photoelectron spectroscopy

1. Introduction

Today, our society is facing serious challenges with population ageing due to an increasing life expectancy and a declining birth rate. Studies show [1] that the cumulative probabilities for the 60+ years of age to reach one-third of the population by this mid-century are 98% in Japan/Oceania, 82% in Western Europe, and 69% in China. One direct consequence would be the increase of economic burden and workload for the healthcare system. Meanwhile, patients will expect longer queue time for doctor visits, medical examinations and treatments. In many cases, patients can recover naturally and in fact do not need any medical treatments or surgeries. However, hospital visits are still necessary for doctor to gather sufficient information and make correct diagnostics.

Point-of-care (POC) devices, which can analyze samples, *e.g.*, blood, without involving the use of laboratory staff and facilities and provide results within minutes, would be an ideal solution to the aforementioned issues related to an ageing society. As illustrated in Figure 1(a), with such a device, patients could, for example, perform self-tests at home and receive instantaneous on-line consultancy for whether a doctor visit for further treatment is necessary or not. As a result, a significant reduction in the frequency of hospital visits, burden on the transportation infrastructure as well as on the environment, lost work time for the patients, etc. could be achieved. The efficiency of the healthcare system will also be improved [2]. Meanwhile, POC devices can be very helpful in situations where data is needed immediately, for example on board an ambulance, if a patient needs to be treated as soon as possible. In some applications, such as measurement of the glucose level, where samples degrade rapidly, on-site analysis using POC devices could also be very useful.

The analytical targets for POC devices can be proteins, metabolites, nucleic acids, and pathogens [2]. The protein assay targets disease specific protein markers such as glycated hemoglobin (HbA1c) for diabetics, C-reactive protein (CRP) for inflammation including cardiovascular disease, and prostate-specific antigen (PSA) for prostate cancer [3]. The POC devices utilize immunoassay technology such as antigen-antibody binding to capture protein targets. Metabolites are products of chemical processes, and their levels are often diagnostic indicators of disease. Common metabolites targeted by POC devices include glucose, cholesterol, triglycerides, creatinine, lactate, ammonia, urea as well as simple ionic blood chemicals, such as H^+,

Na^+, and K^+ [4]. Biosensors for glucose, which enable diagnosis and management of diabetes mellitus afflicting more than 125 million people worldwide [5], account for approximately 85% of the entire biosensor market [6]. A nucleic acid assay targets DNA or RNA to measure genetic details of a patient or unique nucleic acid sequences of invading pathogens. The target nucleic acid from the sample is specifically captured on a substrate through hybridization with a pre-immobilized, complementary "probe" DNA. In addition, pathogens can be diagnosed by nucleic acid identification [7], and in some cases, such as tuberculosis [8], can be diagnosed via specific antibodies presenting in an infected host.

As shown in Figure 1.1(b), an ideal POC device usually consists of three components: (i) microfluidic features to control sample preparation, flow rate, reagent mixing, and reaction time associated with surface binding, (ii) a sensitive surface functionalized with "probes" to capture targets, and (iii) a signal transducer to read the binding signal [9]. The device should be portable, low-cost, highly sensitive and selective, and provide fast response. Microfluidics has been a significant component in recent research of POC devices but is beyond the focus of this thesis. The methods to read out signals from bound targets fall into two categories: labeled and label-free technologies [9–13]. For labeled detections, targets are labeled with different tags such as a reduction-oxidation (redox) label [14] for electrochemical detection, a chromophore [15], a fluorophore [16], or particles [17] (quantum dot [18] or noble metal [19]) for optical detection, and magnetic particles [20] for magnetic detection. For example, pregnancy tests use antibody-based binding of gold nanoparticles to produce a colored line if sufficient human chorionic gonadotropin (hCG) is present in the urine sample [21]. The major concern for labeled detections is that the labeling step can drastically change the binding properties of biomolecules. Meanwhile, the yield of target-label coupling reactions is highly variable which makes it difficult to quantify the bound targets whose number is assumed to correspond to the amount of labels [13]. On the other hand, label-free sensors directly detect the changes in physical properties of the functionalized surface resulting mainly from the

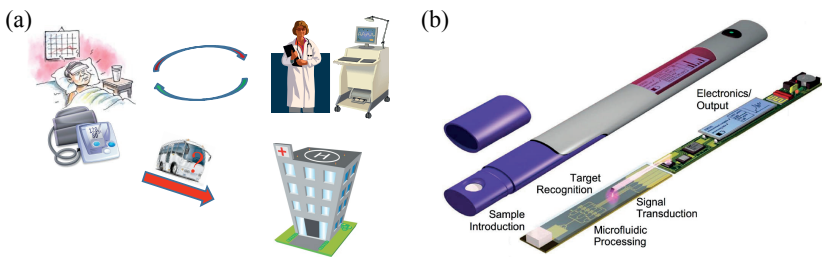

Figure 1.1. (a) Concept of self-diagnostics at home using POC devices and (b) structure of an ideal POC device [2].

binding of target biomolecules. For example, biomolecular incorporation may lead to changes in surface electrical potential, mass (resonance frequency), and dielectric constant close to the surface, which can be measured by ion selective field-effect transistor (ISFET) [22–25], quartz crystal microbalance (QCM) [26, 27], and surface plasmon resonance (SPR) [11, 28, 29] sensors, respectively. Besides the saving of laboratory time and expenses related to the labeling step, label-free sensors can detect binding events in real-time, allowing for the determination of affinity constants by fitting the response curve [30], which is generally not possible for labeled detections.

Among the various label-free technologies, the ISFET has attracted most attention because of its potential advantages such as small size and weight, fast response, high reliability, low output impedance, and the possibility of on-chip integration of sensor arrays and a signal processing scheme with the prospect of low-cost mass production of portable microanalysis systems [23]. By displaying the number of publications as well as some historical landmarks along the path of the development of the ISFET-based sensors, Figure 1.2 presents an attempt to map out the vast scientific and technological advancements during the past four decades. The pace in scientific publications has apparently been accelerated since year 2005. On the application side, since its invention in 1970 by Bergveld [31], the ISFET has been widely used for detection of inorganic ions [22, 23, 32–34]. In particular, ISFET based proton sensors have been successfully implemented in a novel non-optical genome sequencing technology which is now commercially available from Ion Torrent by Life Technologies [35]. Despite the practical difficulties regarding the detection of biological samples such as protein and DNA [23, 36–38], ISFET-based biosensors have been extensively studied in the past decades, and the research interest shows no sign of diminishing even today.

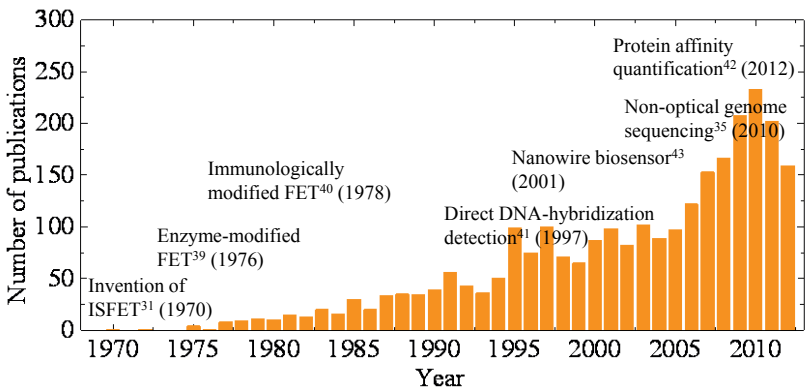

Figure1.2. Number of publications and major historical landmarks during the development of ISFET-based sensors [31, 35, 39–43].

The main challenge in using ISFETs to detect biomolecules is that biomolecules carry zero net charge due to the screening effect of ions in electrolyte, unless they can approach the ISFET gate surface to a distance of Debye length [36–38], which is about 1 nm in typical physiological solutions. Therefore, the binding signal, *i.e.*, surface potential shift, as a result of charge redistribution within the electrical double layer (EDL) can be too weak to detect.

In 2001, a research group from Harvard University proposed the concept of using silicon nanowire field-effect transistors (SiNWFETs), to overcome the sensitivity limitation of planar ISFET-based biosensors [43]. The advantages of SiNWFETs as claimed by the authors are [43]: first, increased sensitivity because biomolecular bindings will lead to depletion or accumulation of carriers in the "bulk" of the nanowire versus only the surface region of an ordinary planar ISFET device; second, possibility to fabricate dense sensor arrays because of the small size of a nanowire. It is reasonable to argue that a nanowire device is more sensitive than a large-area planar device to local surface potential changes induced by biomolecular binding, especially in the situation where the sample concentration is low and the biomolecules are sparsely distributed on the surface [44]. However, the claimed advantage of a nanowire device over a large-area planar device in detection of biomolecules of extremely low sample concentrations has been challenged [45]. In these cases, response time is limited by transportation or surface reaction of biomolecules to the nanowire surface, and hours or even days would be necessary between two consecutive binding events at fM sample concentrations [45]. These time scales are in sharp contradiction to the reported fast response on the order of 10 seconds by several groups [46–49]. Despite the intense debate over the physical explanation of observed biomolecular binding signals [36–38], researchers demonstrated that affinity parameters of immunological reactions could be determined by SiNWFET sensors [42].

Although the operation of ISFETs has been extensively investigated during the past decades [22], the understanding of SiNWFETs operating in electrolyte is still poor. The primary focus of this thesis is to build a platform based on SiNWFETs integrated with microfluidics which is capable of multiplex sensing of different biomolecules. The main efforts have been devoted to understanding the operation mechanisms of SiNWFETs in electrolytic environments, including gate coupling, device stability, possible sources of false signals, and sensitivity to surface potential variations. For sensitivity characterization, *p*H sensing has been used as a model system due to its simplicity and better understanding in the literature. Substantial work has been performed to investigate the stability issues related to the use of an inert-metal gate electrode. Instead of antibodies, short artificial proteins (Affibody molecules) have been used as capture probes during our protein sensing ex-

periment in order to bring the target proteins to the sensor surface within the Debye screening length.

The thesis is organized as follows. Chapter 2 introduces the theoretical background of the ISFET with a special focus on the physical model describing its *p*H sensitivity as well as its difficulties in biomolecular sensing. This discussion also motivates the introduction of graphene-based sensors as a new possibility in field-effect sensing. Chapter 3 describes the experimental details, including the fabrication process of SiNWFETs, on-chip integration of microfluidics, device characterization in the presence of electrolyte, surface functionalization, *p*H and biomolecular sensing, and the design of a multiplex sensing platform. A brief account of precautions in the characterization of graphene-FET is provided. An overview of the appended papers is included in Chapter 4 and the thesis is concluded with an extensive summary and a future outlook in Chapter 5.

2. Theoretical Background

The concept of field-effect sensing was introduced by Bergveld [31] in the early 1970's, marked by the invention of ISFET. It was found that the concentration of Na^+ ions in an electrolyte can be detected by monitoring drain-to-source current (I_{DS}) of an ISFET at constant *p*H. In fact, ISFET is similar to a metal-oxide-semiconductor field-effect transistor (MOSFET), cf. Figure 2.1(a) for a schematic cross-section of an *n*-channel MOSFET device, with the gate electrode separated from the chip in the form of a reference electrode inserted in an electrolyte that is in direct contact with the gate insulator [22]. As shown in Figure 2.1(b), when the gate insulator of ISFET is in contact with an electrolyte, EDL is established at the electrolyte/gate insulator interface with a potential drop (φ_s) over it. φ_s is determined by the surface charge density (σ_s) on the gate insulator and the differential capacitance (C_d) of the EDL, *i.e.*, $\varphi_s=\sigma_s/C_d$. A surface reaction or biomolecular binding occurring on the gate insulator will lead to changes in σ_s and φ_s that can be detected by monitoring the threshold voltage shift of the ISFET, ΔV_{TH}.

In this chapter, the operation mechanism of the ISFET is briefly introduced. First, the basic MOSFET device physics and the dependence of

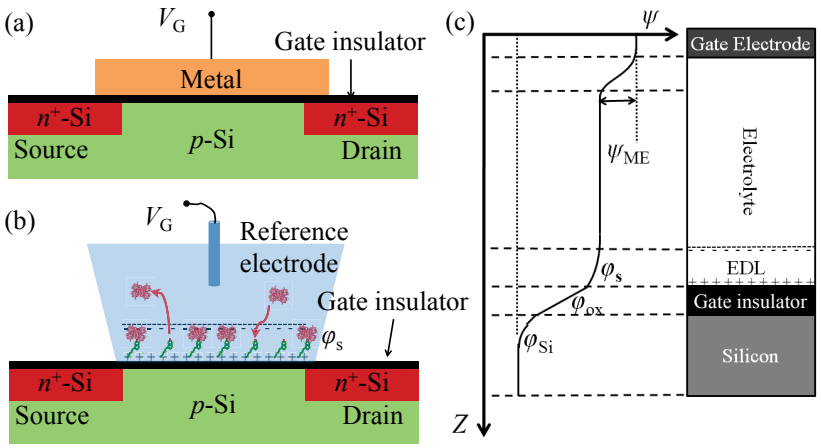

Figure 2.1. Schematic representations of (a) an n-type MOSFET, (b) an ISFET with functionalized gate insulator and bound biomolecules, and (c) the potential distribution in an ISFET.

ISFET V_{TH} on φ_s are presented. Then, the formation of the EDL at the solid/electrolyte interface is described and the influence of chemical reactions and biomolecular binding on φ_s is discussed. Furthermore, the metal/electrolyte interface is analyzed to illustrate the crucial importance of a reference electrode in achieving stable and reliable sensing results. Finally, a graphene-based capacitor is discussed as an attractive sensor for a simultaneous determination of changes in σ_s and C_d.

2.1. The threshold voltage of an ISFET

A MOSFET is a three-terminal electronic switch, as seen in Figure 2.1(a). The state change from ON to OFF, and vice versa, is controlled by the vertical electrical field induced by gate voltage (V_G). According to device physics, the function of V_G is to modulate the energy barrier and conductance in the channel region of the device, thereby controlling the electrical current flowing from the source to the drain. For an *n*-channel MOSFET as seen in Figure 2.1(a), when V_G is lower than its V_{TH}, the device acts like two back-to-back *p*-*n* diodes with a large energy barrier in between. As a result, the device can only conduct a small leakage current. When a positive V_G is sufficiently large ($>V_{TH}$), the energy barrier is suppressed, leading to the formation of a surface inversion layer (*n*-channel) in the channel at the SiO_2/silicon interface. Now, a large current can flow from the source to the drain. The conductance and therefore I_{DS} of the channel can be modulated by varying V_G [50], giving rise to the I_{DS} versus V_G curves in Figure 2.2.

For an *n*-channel MOSFET, V_{TH} can be expressed as:

$$V_{TH} = \frac{\emptyset_M - \emptyset_{Si}}{q} - \frac{Q_f + Q_m + Q_{ot}}{C_{ox}} + 2\psi_B + \frac{\sqrt{4\varepsilon_{Si} q N_A \psi_B}}{C_{ox}}. \qquad (2.1)$$

In Eqn. (2.1), the first term is the work function difference between the gate electrode (Φ_m) and the silicon substrate (Φ_{Si}), the second term is the potential drop caused by fixed oxide charge (Q_f), mobile ionic charge (Q_m), and oxide trapped charge (Q_{ot}) in the gate oxide, the third term is the voltage required to invert the surface region of the substrate, and the last term is the voltage required to compensate for the depletion charge. When V_G is higher than V_{TH} and for a small drain voltage (V_D), I_{DS} is dominated by the drift current given by:

$$I_{DS} \cong \frac{W}{L} \mu_n C_{ox} (V_G - V_{TH}) V_D, \qquad (2.2)$$

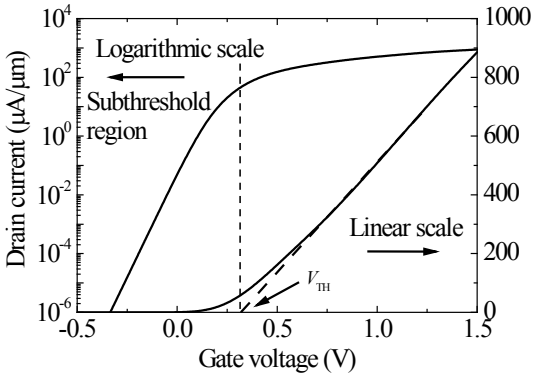

Figure 2.2. I_{DS}-V_G characteristic of an n-channel MOSFET in both logarithmic and linear scales.

where μ_n is the effective electron mobility. If V_D is increased to V_{Dsat} where the device reaches its pinch-off point, I_{DS} becomes independent of V_D and stays at constant I_{DSsat} given by:

$$I_{\mathrm{DSsat}} \cong \frac{W}{2L}\mu_{\mathrm{n}}C_{\mathrm{ox}}(V_{\mathrm{G}} - V_{\mathrm{TH}})^2. \tag{2.3}$$

When V_G is below V_{TH}, the channel is only weakly inverted and the corresponding I_{DS} is called the subthreshold current, which is diffusion limited and decreases exponentially with V_G [51, 52]:

$$I_{\mathrm{DS}} \sim e^{2.3\frac{V_{\mathrm{G}}-V_{\mathrm{TH}}}{SS}}, \tag{2.4}$$

where *SS* is the subthreshold slope of the MOSFET.

For the ISFET, the contributions from metal/electrolyte (φ_{ME}) and electrolyte/oxide (φ_s) interfacial potentials, as seen in Figure 2.1(c), should be considered, and the expression of its V_{TH} becomes [22, 33]

$$V_{\mathrm{TH}} = E_{\mathrm{ME}} - \varphi_{\mathrm{s}} + \chi^{\mathrm{sol}} - \frac{\emptyset_{\mathrm{Si}}}{q} + \frac{Q_{\mathrm{f}}+Q_{\mathrm{m}}+Q_{\mathrm{ot}}}{C_{\mathrm{ox}}} + 2\psi_{\mathrm{B}} + \frac{\sqrt{4\varepsilon_{\mathrm{Si}}qN_{\mathrm{A}}\psi_{\mathrm{B}}}}{C_{\mathrm{ox}}}. \tag{2.5}$$

E_{ME} is the electrode potential for the metal/electrolyte half-cell relative to the vacuum potential, which can be calculated by adding 4.7 V to its potential relative to the standard hydrogen electrode potential [53]. χ^{sol} is the surface dipole potential of the solvent and has a constant value [54]. A reference gate electrode is usually used to provide a stable E_{ME} so that φ_s is the only

variable in Eqn. (2.5). As described earlier, φ_s depends on the surface reaction or biomolecular binding occurring on the gate insulator. The I_{DS} expressions for an ISFET are the same as the ones for a MOSFET, *i.e.*, Eqns. (2.2) and (2.4). During operation, an ISFET can be biased at constant V_G and a change to V_{TH} caused by variations of φ_s can be detected by monitoring its I_{DS} in real-time. Clearly, higher current sensitivity, *i.e.*, $\Delta I_{DS}/I_{DS}$, can be obtained if the bias point is in the subthreshold region where I_{DS} is exponentially dependent on $(V_G\text{-}V_{TH})$.

2.2. Metal/electrolyte junction and reference electrode

As illustrated in the potential diagram of the ISFET, *i.e.*, Figure 2.1(c), the metal/electrolyte junction potential (φ_{ME}) should be stable during operation. Only if this is so can the electrolyte potential ψ_{EL} be stable and thus ΔV_{TH} of the sensor is solely related to $\Delta\varphi_s$ caused by a surface reaction or biomolecular binding occurring on the gate insulator. A stable ψ_{EL} is normally achieved by applying the V_G to a reference electrode [22] that possesses a well-defined electrode reaction thus yielding a stable electrode potential.

When a metal electrode is in contact with an electrolyte, electrochemical reactions and exchange of species, *i.e.*, electrons and ions, can take place between the metal and electrolyte phases due to the chemical potential (μ_j) difference between them. This leads to build-up of an electrical potential (φ_{ME}) across the interface. The reaction reaches equilibrium when the electrochemical potentials ($\overline{\mu_j}$) of the species in the metal and electrolyte phases are equal [55]. $\overline{\mu_j}$ of species j depends on μ_j of species j and the electrical potential (ψ) in the phase containing species j:

$$\overline{\mu_j} = \mu_j \pm z_j F\psi. \tag{2.6}$$

Here z_j is the number of elementary charges associate with one ion. The plus sign is valid for cations and the minus sign for anions. For the Ag/AgCl reference electrode, the electrode reaction can be expressed as:

$$\mathrm{AgCl} + e^- \rightleftharpoons \mathrm{Ag} + \mathrm{Cl}^-. \tag{2.7}$$

The species involved in the reaction, *i.e.*, Ag^+ and Cl^-, should have the same electrochemical potentials in the metal and electrolyte phases at equilibrium:

$$\begin{aligned} \mu^{\mathrm{M}}_{\mathrm{Ag}^+} + F\psi_{\mathrm{M}} &= \mu^{\mathrm{E}}_{\mathrm{Ag}^+} + F\psi_{\mathrm{E}} \\ \mu^{\mathrm{M}}_{\mathrm{Cl}^-} - F\psi_{\mathrm{M}} &= \mu^{\mathrm{E}}_{\mathrm{Cl}^-} - F\psi_{\mathrm{E}} \end{aligned} \tag{2.8}$$

In Eqn. (2.8), $\mu^{M}_{Ag^+}$ and $\mu^{E}_{Ag^+}$ are the chemical potentials of Ag^+ in the metal and the electrolyte, respectively, while $\mu^{M}_{Cl^-}$ and $\mu^{E}_{Cl^-}$ are the chemical potentials of Cl^- in the metal and the electrolyte. ψ_M and ψ_E are the electrical potentials in the metal and the electrolyte, respectively. φ_{ME} across the metal/electrolyte interface (in mV), *i.e.,* ψ_E-ψ_M, can be expressed as [55]:

$$\varphi_{ME} = 59.2 \log_{10} a_{Cl^-} + \text{constant}, \tag{2.9}$$

which only depends on the activity of Cl^-, a_{Cl^-}, in the electrolyte. Figure 2.3(a) depicts the structure of an Ag/AgCl reference electrode. Since a_{Cl^-} is constant in the KCl filling solution, φ_{ME} is constant and thus ψ_{EL} in the bulk electrolyte is stable if a constant V_G is applied. A reference electrode is usually bulky as shown in Figure 2.3(b), and difficult to be miniaturized and integrated on-chip. As a result, many researchers turn to inert metals [56–58], such as Pt and Au, as materials for gating the device. However, the lack of a well-defined electrode reaction makes the inert-metal gate electrodes incapable of maintaining a stable φ_{ME} when they are immersed in the electrolytes commonly used for biosensing experiments [59, 60]. Hence, use of inert-metal gate electrodes frequently results in serious stability and reliability issues, which will be further explored later.

2.3. Surface potential at the gate insulator/electrolyte interface

In this section, the explicit expressions for φ_s will be derived. The influence of ion concentrations, *e.g.*, $[H^+]$, and biomolecular binding on φ_s will be discussed.

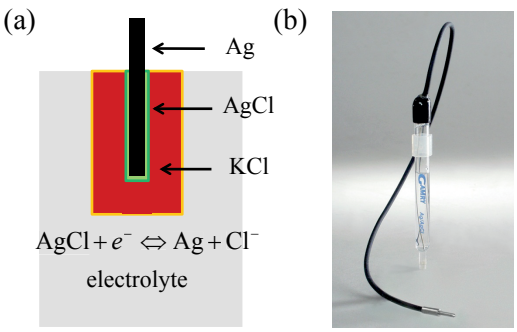

Figure 2.3. (a) Schematic representation of the Ag/AgCl reference electrode structure and (b) photo picture of an Ag/AgCl reference electrode from GAMRY Instruments.

2.3.1. *p*H sensing

Detection of proton concentrations [H^+] or *p*H values in electrolyte is one of the most important applications for ISFETs. Silicon oxide, as the first and perhaps also the most exploited gate insulator material for ISFETs [31], contains a high density of hydroxyl groups, *i.e.*, Si-OH, on the surface. The hydroxyl groups undergo protonation and deprotonation when the oxide is in contact with an aqueous solution, leading to a net σ_s that depends on the chemical equilibrium of the surface reaction. This is the origin of the EDL formation on the oxide surface. According to the site-binding model, the surface reaction taking place at the gate insulator/electrolyte interface can be characterized by two equilibrium constants, K_a and K_b [54]:

$$\text{Si-OH} \leftrightharpoons \text{Si-O}^- + \text{H}^+, \text{ with } K_a = \frac{[\text{Si-O}^-][\text{H}^+]_S}{[\text{Si-OH}]} \tag{2.10}$$

$$\text{Si-OH}_2^+ \leftrightharpoons \text{Si-OH} + \text{H}^+, \text{ with } K_b = \frac{[\text{Si-OH}][\text{H}^+]_S}{[\text{Si-OH}_2^+]}. \tag{2.11}$$

Here $[H^+]_S$ is the surface concentration of H^+ ions and its relationship with the bulk concentration ($[H^+]_B$) can be described by the Boltzmann distribution:

$$[\text{H}^+]_S = [\text{H}^+]_B \exp\left(-\frac{q\varphi_S}{kT}\right) \quad pH_S = pH_B + \frac{q\varphi_S}{2.3kT}, \text{ with}$$
$$pH_S = -\log_{10}[\text{H}^+]_S \quad pH_B = -\log_{10}[\text{H}^+]_B \tag{2.12}$$

The total number density of surface sites (N_S) on the gate insulator is given by:

$$N_S = [\text{Si-OH}] + \left[\text{Si-O}^-\right] + \left[\text{Si-OH}_2^+\right]. \tag{2.13}$$

The parameters K_a, K_b and N_S for the commonly used gate insulator materials are shown in Table 2.1. Combining Eqns. (2.10)-(2.13), the relationship between σ_S and $[H^+]_S$ can be derived:

$$\sigma_S = q\left(\left[\text{Si-OH}_2^+\right] - \left[\text{Si-O}^-\right]\right) = qN_S\left(\frac{[\text{H}^+]_S^2 - K_a K_b}{K_a K_b + K_b[\text{H}^+]_S + [\text{H}^+]_S^2}\right). \tag{2.14}$$

The intrinsic buffer capacity β_{int}, which characterizes the capability of the surface to store charge as the result of a small change of $[H^+]_S$, is defined as:

$$-q\beta_{int} = \frac{\partial \sigma_S}{\partial pH_S}. \tag{2.15}$$

This shows that β_{int} only depends on the intrinsic properties of the surface, *i.e.*, N_S, K_a, and K_b, and is different for different gate insulators.

Table 2.1. Equilibrium constants and site densities for different materials [54]

Material	pK_a	pK_b	pH_{pzc}	N_S (cm^{-2})
SiO_2	6	-2	2	5×10^{14}
Al_2O_3	10	6	8	8×10^{14}
Ta_2O_5	4	2	3	10×10^{14}

An equal amount of charge σ_{EDL} with opposite polarity accumulates in the electrolyte side of the EDL due to the charge neutrality requirement [61]. In detail, the EDL is actually made up with several layers as seen in Figure 2.4. A Helmholtz or Stern layer containing solvent molecules and sometimes specifically adsorbed species is located closest to the oxide surface. The locus of the electrical centers of the absorbed ions and molecules is called the inner Helmholtz plane (IHP), which is at a distance x_1 from the oxide surface. The solvated ions that counterbalance the surface charge σ_s can approach the oxide surface only to a distance x_2. The locus of the center of these nearest solvated ions is called the outer Helmholtz plane (OHP). The solvated counter ions extend from the OHP into the bulk of the electrolyte, forming a diffuse layer. The interaction between surface charge and solvated ions in the diffuse layer is through the electrostatic force. Therefore, a thinner diffuse layer is expected in an electrolyte with a higher ionic strength due to a stronger ion screening effect. The differential capacitance of the EDL, *i.e.*, C_d, can be obtained from the Gouy-Chapman-Stern (GCS) model [61]:

$$\frac{1}{C_d} = \frac{x_2}{\varepsilon_s \varepsilon_0} + \frac{1}{\sqrt{\frac{2\varepsilon_s \varepsilon_0 z^2 q^2 n^0}{kT}} \cosh\left(\frac{zq\phi_2}{2kT}\right)}, \tag{2.16}$$

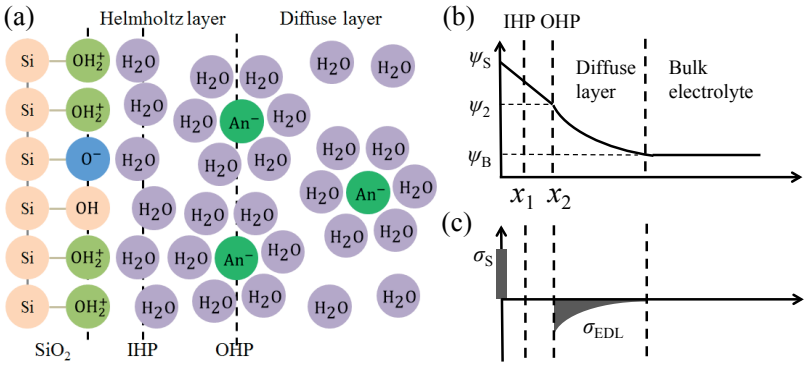

Figure 2.4. (a) GCS model of the EDL in the absence of specific adsorption, (b) potential, and (c) charge distributions at the oxide/electrolyte interface [54], [61].

where ε_S is the dielectric constant, z and n^0 are charge magnitude and number concentration of ions in a z:z electrolyte, respectively. Combining Eqns. (2.12) and (2.15), the dependence of φ_S on $p\mathrm{H}_B$ can be obtained as:

$$\frac{\partial \varphi_S}{\partial p\mathrm{H}_B} = \frac{\partial \varphi_S}{\partial \sigma_S} \cdot \frac{\partial \sigma_S}{\partial\left(p\mathrm{H}_S - \frac{\varphi_S}{2.3kT}\right)} = -2.3\frac{kT}{q}\alpha, \text{ with}$$
$$\alpha = \frac{1}{1+\frac{2.3kTC_d}{q^2\beta_{int}}}. \qquad (2.17)$$

α is a dimensionless sensitivity parameter varying between 0 and 1. For gate insulators with a large β_{int} in contact with electrolyte with low C_d, α will be close to 1 and therefore a high pH sensitivity can be expected. Eqn. (2.17) also reveals the upper bound of the pH sensitivity of an ISFET, *i.e.*, the so-called Nernstian limit (59.2 mV/pH at room temperature), when α is equal to 1. Figure 2.5 shows the response of ISFETs with different gate materials [22]. Ta_2O_5 has the largest β_{int} and is the best gate material for an ISFET pH sensor, as demonstrated by its near ideal Nernstian response, *i.e.*, 59.2 mV/pH, at 298 K and inertness to changes of ionic strength.

2.3.2. Protein detection

The possibility of using ISFETs to directly monitor antibody-antigen interactions has attracted many attempts to build biosensors where the recognition process takes place on the gate insulator surface. Proteins are composed of one or more polypeptide molecules that are a linear sequence of repeating units, *i.e.*, amino acids [62]. The charge of a protein depends mainly on its amino acid composition and the pH level of electrolyte. Each protein has a characteristic pI, which is the pH at which the protein has no net charge. At a

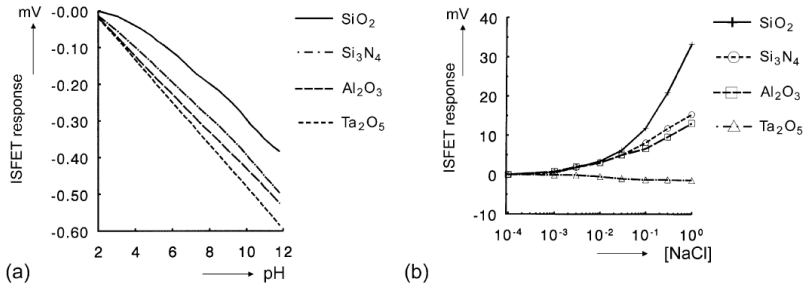

Figure 2.5. ISFET response to change of (a) pH at constant 0.1 M tetrabutylammonium chloride (TBACl) concentration and (b) NaCl concentration at constant pH [22].

*p*H lower than its *p*I, the protein carries a net positive charge; for *p*H higher than its *p*I, the protein carries a net negative charge [63]. Therefore, it is assumed that the binding of antigens to their antibodies immobilized on the gate insulator should lead to a detectable $\Delta\varphi_s$ resulting from $\Delta\sigma_s$.

However, whether it is possible or not to measure the charge redistribution induced by protein binding in an ISFET has been intensely debated. Figure 2.6(a) shows the potential profile at the gate insulator/electrolyte interface and its overlap with the bound protein molecules. The thickness of the EDL is characterized by the Debye length (κ^{-1}), which is defined as the distance from the oxide surface extending into the electrolyte until the external electrical field is screened [37]:

$$\kappa^{-1} = \sqrt{\frac{\varepsilon_s \varepsilon_0 kT}{2q^2 P}}, \text{ with } P = \frac{1}{2}\sum c_i z_i^2 \qquad (2.18)$$

Mathematically, κ^{-1} is the distance extending into the electrolyte at which the electrical potential is decreased to 1/e of its strength at the oxide surface as schematically shown in Figure 2.6(a). *P* in Eqn. (2.18) represents the ionic strength of the electrolyte, c_i and z_i are the concentration and valence of ion *i*. However, the dimensions of antibodies are ca. 10 nm, which is much larger than $\kappa^{-1} \approx 1$ nm for typical physiological solutions. Hence, the charge carried by the bound biomolecules located outside the Debye length cannot be "seen" since it is screened by the counter ions. It is possible to achieve a certain level of overlap between bound biomolecules and the EDL by reduc-

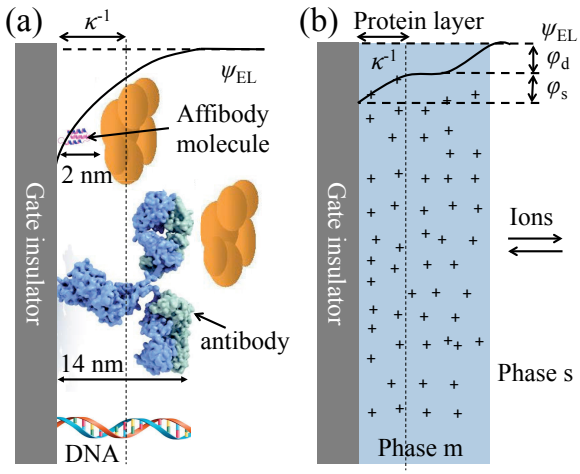

Figure 2.6. Schematic representations of (a) overlapping of the EDL with target biomolecules when antibody, ssDNA, and Affibody are used as receptors and (b)Donnan equilibrium [37].

ing the ionic strength, but this could also lower the immunological binding affinity.

Another complication with protein detection is that it is difficult to determine the actual amount of charge carried by the bound proteins [37]. The charge density of a protein depends on the *p*I of the protein and the *p*H level of the surrounding electrolyte. However, the *p*H levels in the bulk electrolyte, *i.e.*, pH_B, and at the gate insulator surface, *i.e.*, pH_s, are different, as described by Eqn. (2.12). For example, the difference between pH_B and pH_s is about 2 with φ_s=100 mV. Therefore, it is also difficult to determine the protein charge polarity when the protein is close to the gate insulator surface.

2.3.3. Donnan equilibrium

Many researchers have used the Donnan effect to explain the observed protein binding signals [23, 36–38]. In the Donnan equilibrium, protein capture probes are considered as a membrane deposited on the gate insulator. As shown in Figure 2.6(b), the protein membrane and solution can be treated as two phases, *i.e.*, phase m and s [37]. Assuming that small ions can diffuse freely between phase m and s, there will be a difference in ion concentration between the two phases as a result of the presence of fixed charges in the protein membrane and a potential drop, the Donnan potential φ_d, across the interface of the two phases. At equilibrium, the electrochemical potentials of the ions in phase m and s should be equal and φ_d is given by [36, 37]:

$$\varphi_d = \psi_m - \psi_s = \frac{kT}{q} \ln \frac{\sqrt{4c_s^2 + c_x^2} + c_x}{2c_s}, \tag{2.19}$$

where ψ_m and ψ_s are the electrical potentials in phase m and s, respectively, c_s is the salt concentration in the electrolyte, and c_x represents the effective fixed charge density in the protein membrane.

The binding of target proteins to the receptors will lead to a change of c_x and subsequent a change of φ_d. Meanwhile, the *p*H level in phase m will also shift as a result of the change of φ_d, which is $\Delta pH = q\Delta\varphi_d/2.3kT$. According to Eqn. (2.19), $\Delta\varphi_d$ is more significant with lower c_s. The total response of the ISFET to protein binding is a combined effect of $\Delta\varphi_s$, as a result of the *p*H change in phase m, and $\Delta\varphi_d$ at the protein membrane/solution interface. By including Eqn. (2.17), ΔV_{TH} of ISFET as a result of protein binding can be obtained:

$$\Delta V_{TH} = (1 - \alpha)\Delta\varphi_d. \tag{2.20}$$

Clearly, V_{TH} of ISFET is *not* affected by protein binding if the ISFET shows an ideal Nernstian behavior (α=1), because $\Delta\varphi_d$ is fully compensated for by

$\Delta\varphi_s$ as a result of the change of membrane *p*H [37]. However, if the ISFET shows a non-ideal Nernstian response (α<1) then non-zero ΔV_{TH} can be expected upon protein binding.

2.3.4. DNA detection

DNA detection is normally based on a DNA hybridization process, *i.e.*, the target single-stranded DNA (ssDNA) is identified by a probe ssDNA immobilized on the gate insulator surface of the ISFET [41, 56]. The probe ssDNA can form a double-stranded DNA (dsDNA) helix structure with its complementary target ssDNA with a high affinity and specificity, while non-complementary nucleic acids lack such affinity. DNA molecules have a negatively charged phosphate backbone and can be considered as a circular cylinder (about 1.5~2 nm in diameter) with charges evenly distributed on the cylindrical surface [64]. DNA detection with an ISFET faces the same difficulty as protein detection due to charge screening by small inorganic counterions. However, the DNA molecules have a unique structure, *i.e.*, the length of a nucleotide, or base, is about 0.34 nm [65]. Even in physiological solutions, several bases could fit into the EDL with a κ^{-1}~1 nm and therefore it is possible to detect the charge redistribution at the gate insulator/electrolyte interface resulting from the hybridization process [23].

2.3.5. Affibody molecule as receptor

Protein detection has been severely hindered by the Debye screening effect in electrolytes. As shown in Figure 2.6(a), when antibodies are used as receptors, the bound targets are most likely outside the Debye length because the size of antibodies is much larger (ca.10 nm) than $\kappa^{-1}\approx$1 nm. Affibody molecules are engineered antibody mimetics with a much smaller size (about 2 nm) compared to the antibodies [66]. The molecular weight of Affibody molecules is about 6 kDa while it is about 150 kDa for antibodies [67]. In spite of its small size, the binding sites of Affibody molecules are similar to those of antibodies [66]. Meanwhile, Affibody molecules have robust physical properties and can withstand extreme *p*H and elevated temperature [67]. The advantage of using Affibody molecules instead of antibodies as receptors for protein detection is clearly illustrated in Figure 2.6(a). The significantly smaller size of Affibody molecules can increase the chance for the bound targets to overlap with the EDL, thus facilitating protein detection.

2.4. Graphene based field-effect sensor

As described earlier, the ISFET-based biomolecular sensors detect $\Delta\varphi_s$ at the gate insulator/electrolyte interface; $\Delta\varphi_s$ is jointly determined by $\Delta\sigma_s$ and ΔC_d,

since the incorporation of biomolecules into the EDL will most likely also alter the dielectric constant within the EDL and thus lead to a change in C_d [68]. As a result, the quantification of bound biomolecules would require a sophisticated physical model with independent inputs regarding dielectric constant and charge distribution within the EDL. Unfortunately, the current-voltage (*I-V*) measurement on ISFET is incapable of yielding sufficient independent information [69]. On the other hand, capacitance-voltage (*C-V*) method can, in principle, register not only $\Delta\varphi_s$ but also ΔC_d induced by the biomolecular binding [33, 70]. This can then lead to a simultaneous determination of the charge polarity and density of the bound biomolecules through simple physical relations [71, 72]. However, for an ISFET using SiO_2 as the gate insulator, it is usually difficult to accurately determine ΔC_d since C_G is dominated by C_{ox} that is in series connection with C_d; C_{ox} is about 0.35 $\mu F/cm^2$ for a 10-nm thick SiO_2 film while C_d ranges from 10 to 40 $\mu F/cm^2$ dependent on the ionic strength in the electrolyte. A graphene-based field-effect sensor can overcome the aforementioned difficulty by having its channel in direct contact with electrolyte, *i.e.*, without gate insulator. Hence, C_G of the sensor can be viewed as a series connection of C_d and the quantum capacitance (C_q) of graphene. C_q is determined by the density of states (DOS) at the Femi level and is reported to have a minimum value of 7 $\mu F/cm^2$, which is close to C_d [73]. Therefore, *C-V* measurements on the graphene-based field-effect capacitor sensor should be able to simultaneously yield $\Delta\varphi_s$ and ΔC_d resulting from the biomolecular binding. It could be noted that using graphene-based devices for electronic sensing is a relatively young field [74, 75], but the number of publications related to this topic is rapidly rising.

2.5. From planar ISFET to nano ISFET

2.5.1. Sensitivity considerations

The introduction of nano ISFETs based on semiconducting nanowire (NW) was motivated by the large surface-to-volume ratio and high charge sensitivity as proposed by Cui *et al.* in 2001 [43]. A commonly used model for estimating the charge sensitivity of an NW sensor is shown as follows [44]: The conductance G_0 of a cylindrical NW with a diameter of d and a length of L_{NW}, and uniform doping density of N_D, is given by $G_0=q\mu N_D\pi d^2/(4L_{NW})$. If the surface reaction or biomolecular binding leads to a change of surface charge density $\Delta\sigma_s$, the NW will be depleted/accumulated by an equal amount of charge $\Delta Q= \pi d\Delta\sigma_s$. Therefore the response of the NW sensor is given by:

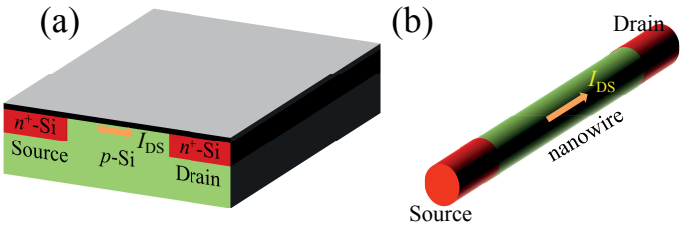

Figure 2.7. 3D sketches of (a) planar ISFET and (b) nano ISFET.

$$\frac{\Delta G}{G_0} = \frac{\frac{\Delta\sigma_S \mu \pi d}{L_{NW}}}{\frac{q\mu N_D \pi d^2}{4L_{NW}}} = \frac{4\Delta\sigma_S}{qdN_D}. \tag{2.21}$$

Equation (2.21) shows that the sensitivity of an NW sensor is inversely proportional to its diameter and doping level. However, there are several imperfections of this model. First, $\Delta\sigma_s$ is actually balanced by the counterions in electrolyte, not by the carriers in the NW. The conductance change of the NW should rather be caused by a V_{TH} shift due to $\Delta\varphi_s$ as described by Eqn. (2.5). Second, the current conduction is along the semiconducting NW surface and the conductance G_0 also depends on V_G.

In fact, if the surface reaction or biomolecular binding takes place uniformly on the gate insulator, the resulting $\Delta\varphi_s$ depends only on the reaction kinetics and the properties of the gate insulator and the electrolyte, irrespective of the type of the underlying signal transducing transistor. Therefore, the resulting ΔV_{TH} for a planar ISFET and a nano ISFET should always be the same. One possible advantage of nano ISFET over a planar ISFET is that when it is gated as a 3D device like a FinFET [76] it can have a better electrostatic control of (or gate coupling efficiency to) the channel, which is represented by a steeper *SS* in the subthreshold region and thus a higher current sensitivity ($\Delta I_{DS}/I_{DS}$) induced by the same ΔV_{TH}.

2.5.2. Response time at low sample concentrations

Shrinking a planar ISFET to a nano ISFET may, however, lead to a significantly increased response time, especially with low sample concentrations. As shown in Figure 2.8, when a fluid carrying biomolecules flows across the sensor, a depletion zone with thickness of δ_s forms due the collection of biomolecules by the sensor. Within this zone, the transportation of biomolecules to the sensor surface is governed by diffusion. The profile of the depletion zone can be well described by two Peclet numbers, Pe_H and Pe_s [45, 77–79]. Pe_H is the ratio between the diffusive and convective time scales and describes the size of the depletion zone compared to the channel height. Pe_s indicates whether the depletion zone is thick or thin compared to the size of

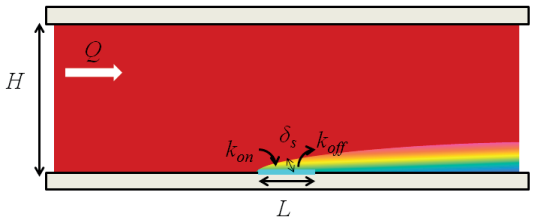

Figure 2.8. A sensor with width L located in a microfluidic channel with height H and volumetric flow rate Q [45].

the sensor. Squires *et al.* compared the response times of microscale and NW sensors at low sample concentrations [45]. The microscale sensor had a width W_s=50 μm and a length L=50 μm, while for the NW sensor W_s=2 μm and L=10 nm. The calculations showed that, with a sample concentration of c_0=10 fM, the maximum biomolecular flux to the sensor surface is about 0.15 molecules per second or one molecule every 7 seconds for the microscale sensor while it is about 8×10^{-5} molecules per second or one molecule every 210 min for the NW sensor.

The response time of the sensors may also be surface reaction limited. The surface concentration b(t) of bound biomolecules obeys the following equations [45]:

$$\frac{\partial b(t)}{\partial t} = k_{\mathrm{on}} c_{\mathrm{s}} [b_{\mathrm{m}} - b(t)] - k_{\mathrm{off}} b(t)$$
$$\frac{b(t)}{b_{\mathrm{m}}} = \frac{\frac{c_0}{K_{\mathrm{D}}}}{1+\frac{c_0}{K_{\mathrm{D}}}} [1 - e^{-(k_{on} c_0 + k_{\mathrm{off}})t}]. \qquad (2.24)$$

c_s is the concentration of target biomolecules at the sensor surface and it is equal to c_0 in the reaction limited case. k_{on} and k_{off} are the association and dissociation rate constants, respectively. The surface concentration at equilibrium, *i.e.*, b_{eq} can be expressed as:

$$\frac{b_{\mathrm{eq}}}{b_{\mathrm{m}}} = \frac{\frac{c_0}{K_{\mathrm{D}}}}{1+\frac{c_0}{K_{\mathrm{D}}}}, \text{ with } K_{\mathrm{D}} = \frac{k_{\mathrm{on}}}{k_{\mathrm{off}}} \qquad (2.25)$$

irrespective of how long the sensor takes to reach equilibrium. If b_m is assumed to be optimized, *i.e.*, $b_m=2\times10^{12}$ sites/cm^2, the number of bound biomolecules N_R^B at equilibrium is 500 and 0.004 for microscale and NW sensors, respectively. Damkohler number (Da=$k_{on}b_m\delta_s/D$), *i.e.*, the ratio of reactive to diffusive flux, indicates the limiting process in the system. If Da<<1, mass transportation is rate limiting while for Da>>1 surface reaction is rate limiting. The microscale sensor with Da≈3 is neither transport limited nor

reaction limited and the time interval between binding events is about 20 s. The NW sensor with Da≈0.03<<1 is, however, reaction limited and the binding proceeds exponentially with a time constant of k_{off}^{-1}≈17 min. Since only 0.004 biomolecules will be bound at equilibrium, the time interval between binding events is thus 17 min/0.004≈3 days for the NW sensor.

3. Experimental Methods

3.1. Fabrication of silicon nanowire transistors

SiNW fabrication schemes fall into two categories: bottom-up and top-down [80, 81]. The bottom-up approach is based on self-assembly growth mechanism. For example, vapor-liquid-solid (VLS) method uses nanoparticles of transition metals (TM) as a catalyst to grow NWs in the presence of a vapor-phase source of the semiconductor [82–85]. In detail, the TM nanoparticles are heated above the eutectic temperature for the selected metal-semiconductor system and a droplet of metal-semiconductor alloy is formed on the nanoparticles. As shown in Figure 3.1, the continued feeding of the semiconductor precursor into the droplet supersaturates the eutectic, leading to nucleation and growth of the semiconductor NW. For SiNW growth, gold nanoparticles are commonly used as the catalyst. Silane (SiH_4), diborane (B_2H_6), and phosphine (PH_3) are reactant sources for silicon, *p*-type and *n*-type dopants, respectively [86]. The diameter of SiNWs grown is determined by the size of the gold nanoparticles. The VLS method is rather simple and mature, and suitable for mass production. However, the as-fabricated SiNWs are randomly distributed on the growth substrate and therefore difficult to manipulate for integration with silicon processes [81]. Moreover, the size of the gold nanoparticles and thereby the diameter of the grown SiNWs cannot be perfectly uniform. In addition, the gold nanoparticles are considered as a major source of contaminants for MOSFETs, which further prevents the application of VLS-grown SiNWs.

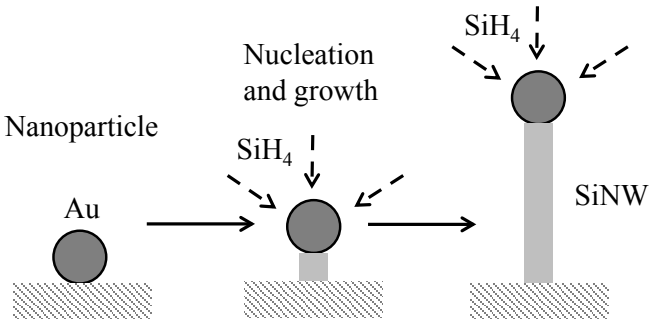

Figure 3.1. Schematics of VLS growth of an SiNW.

On the other hand, the top-down approach uses standard silicon technology to fabricate SiNWs, *i.e.*, the SiNWs are first defined by combining lithography with etching [46, 87–91]. For the top-down approach, the final dimensions of SiNWs are mainly limited by the resolution capability of lithography and the subsequent etching also plays a role. Therefore, the time-demanding electron-beam lithography is frequently used for research purposes [92, 93]. In our work, ordinary photolithography is used mainly to define the fundamental device structures (device-to-device electrical isolation, location and dimension of the 3 terminals – channel, gate, source, and drain) as well as the width of the hardmask on top of the SiNWs. By taking advantage of an extremely high etching anisotropy related to the crystallographic planes of silicon by tetramethylammonium hydroxide (TMAH) [46, 94], we have succeeded in shrinking the micrometer-sized silicon strips down to NWs of width 40 nm with good control. The detailed process flow for the SiNWFET fabrication is schematically illustrated in Figure 3.2. The process started with 100 mm SOI wafers, which comprised a lightly *p*-type doped 260-nm thick Si layer on top of a 150-nm thick buried oxide (BOX). In combination with local oxidation of silicon (LOCOS) for device isolation, a two-step thermal oxidation process was employed to reduce the top Si thickness in the channel region from 260 to about 40 nm while keeping the Si thickness in the source/drain areas unchanged at about 260 nm. The main advantage of retaining a thick Si layer for the source/drain electrodes is the formation of low resistance, reliable contact arms and pads featuring heavily doped Si shunted by a 40-nm thick platinum silicide layer, *i.e.*, PtSi/Si. In detail, the source/drain areas were protected by an oxidation-resistant Si_3N_4 layer, while the channel region was left free of Si_3N_4. The first oxidation led to thinning of the Si thickness in the channel region down to 60 nm. At this point, the Si_3N_4 layer was etched off by concentrated phosphoric acid without affecting the SiO_2 on the rest of the wafer surface. The SiO_2 layer formed during this oxidation step was around 400 nm thick, and it was sufficient to protect the channel region from being implanted during the ion implantation for the source/drain areas. After removal of the 400 nm thick SiO_2, a second oxidation was performed to further reduce the channel Si down to 40 nm as well as to diffuse and activate the dopants in the source/drain areas. The SiO_2 layer formed on the 40 nm thick channel Si layer during this second oxidation step was preserved to serve as the hardmask for the subsequent SiNW channel fabrication. The channel region was first defined by optical lithography and dry etching to form silicon strips 0.3–2.5 μm wide. The strips were then shrunk in width by means of anisotropic wet etching using TMAH. The undercut distance of the SiNW channel as a function of time is shown in Figure 3.3(b). The final width of the SiNWs ranged from 50 nm to 2 μm, depending on the initial dimensions defined by lithography as well as the TMAH etch time. The etchant TMAH erodes Si (111) planes 100 times slower than any other crystallographic planes [46, 94]. Any edge imperfec-

tion that was not aligned to the Si (111) planes would be etched off and therefore the resulting SiNWs should possess a smooth edge profile as seen in Figure 3.3(c). After removal of the SiO_2 layer from the source/drain areas, a 20 nm thick Pt film was deposited by means of electron-beam evaporation. A rapid thermal processing step at 500 °C for 30 s in N_2 atmosphere converted the Pt to PtSi on the source/drain areas while the Pt on SiO_2, *e.g.*, above the channel region, remained intact. Immediately after the silicidation without taking out the wafer from the annealing chamber, a second rapid

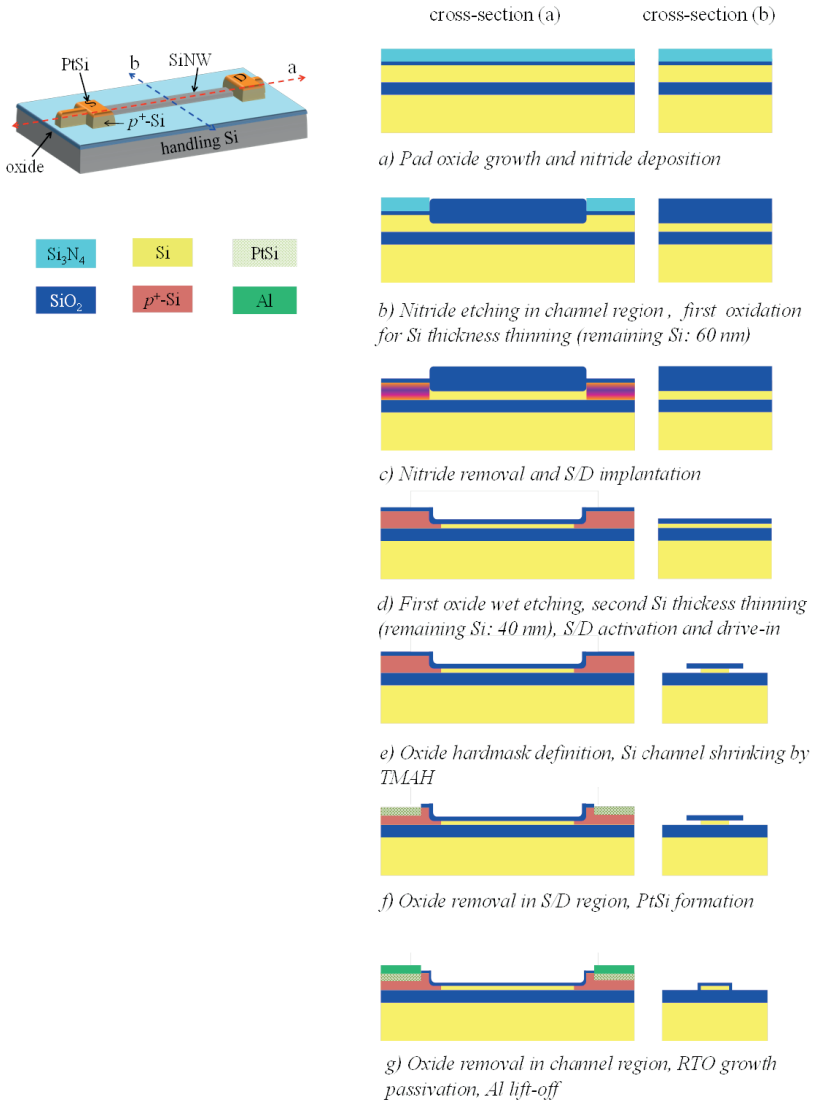

Figure 3.2. Schematic representation of the fabrication process for SiNWFET.

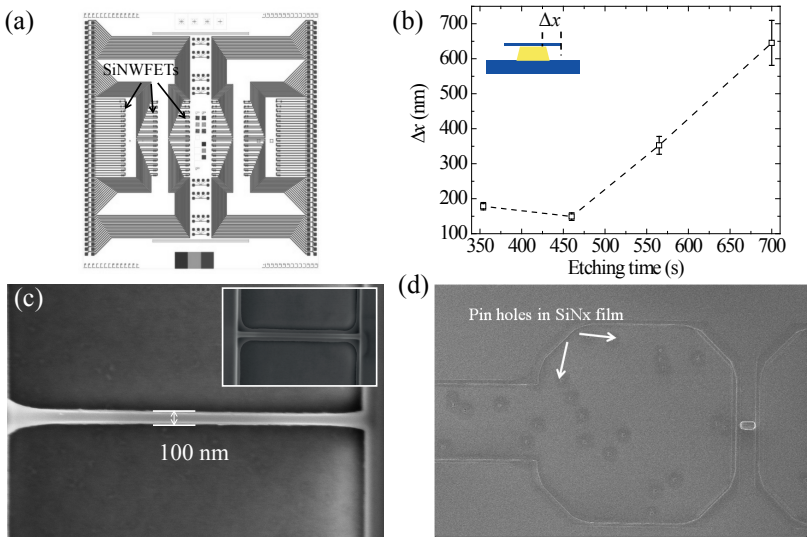

Figure 3.3. (a) Chip layout showing 6 columns of SiNWFETs. Each column contains 16 SiNWFETs with different channel dimensions. (b) Undercut distance (Δx) as a function of TMAH (25%) etching time at 90 °C, SEM images of (c) a 100 nm wide SiNW before (insert) and after hard-mask removal and (d) pinholes in PECVD SiN_x.

thermal processing step at 600 °C for 60 s in O_2 atmosphere led to the formation of SiO_2 on top of the freshly formed PtSi, but not on the Pt surface. This selective nature for oxidation is critical for the self-alignment formation of PtSi as it protects the PtSi from being attacked by aqua regia for removal of Pt from the SiO_2 surface [95].

After the unreacted Pt film was stripped off followed by the oxide removal from the PtSi surface, the SiNWFETs were ready for electrical characterization, which was performed at room temperature on a probe-station using an HP4156A precision semiconductor parameter analyzer. The transfer characteristics (I_{DS}-V_G) of the SiNWFETs with different channel dimensions measured in dry atmosphere are shown in Figure 3.4(b). All transistors exhibit a typical *p*-type accumulation behavior, with a low off-state current (I_{off}) at 10^{-13} A level, while the on-state current (I_{on}) depends on the CW/CL ratio. The hole mobility extracted from the I_{DS}-V_G curves is 130 $cm^2/V^{-1}s^{-1}$.

SiNWFETs need to be passivated in order to avoid leakage current conduction through the electrolyte when operating in electrolyte. Silicon nitride (SiN_x) films prepared by means of plasma-enhanced chemical vapor deposition (PECVD) have been widely used for passivation in biosensor applica-

(a)

CW \ CL	1	2	4	10	20	50	95
0.25		■					
0.30		■					
0.35		■	■				
0.40		■	■	■			
0.50	■	■	■	■	■	■	■
2.00			■	■			

(b)

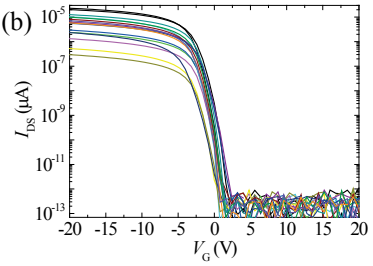

Figure 3.4. (a) 16 SiNWFETs with different channel lengths (CL) and widths (CW) defined by photo lithography (all units in μm) and (b) I_{DS}-V_G curves of the 16 SiNWFETs measured after PtSi formation (before passivation and metallization).

tions [47, 56, 86]. However, the low temperature grown PECVD SiN_x films may contain pinholes as shown in Figure 3.3(d) through which electrolyte can easily penetrate, thus forming leakage current paths. Meanwhile, the SiN_x plasma etching for exposing the SiNW to electrolyte is likely to damage the top and sidewall surfaces of the SiNW, leading to device performance deterioration [46, 96]. Here, we developed a process scheme which uses rapid thermal oxidation (RTO) to grow a thin layer of oxide on the entire structure for simultaneous passivation of the SiNW channel as well as PtSi/Si source/drain electrodes. In detail, after the formation of PtSi, the chips were annealed in O_2 at 800 °C for 5 min to grow a thin oxide layer on SiNWs as well as on PtSi. It was demonstrated that the oxide passivation grown by RTO significantly reduced the leakage current and led to well performing SiNWFETs with a large on-to-off current ratio. More detailed information about the RTO passivation process can be found in Paper I. After passivation, the oxide on the pads placed along the chip edges, as seen in Figure 3.3(a), was removed by wet etching. A 300-nm thick Al layer was then deposited on the pads via electron-beam evaporation and lift-off. Till now, the SiNWFET fabrication is finished and ready for integration with microfluidics channels.

3.2. Sample delivery

Fast sample delivery to the sensor surface is essential in biosensor applications. In this thesis, two delivery methods were used: first, a polydimethylsiloxane (PDMS) container glued onto the chip with sample addition by pipetting; second, a microfluidic system with sample driven by syringe pumps and directed by microfluidic channels.

3.2.1. The PDMS container delivery method

The measurement setup with the PDMS container is shown in Figure 3.5. The container is glued onto the chip while the contact pads placed along the chip edges are outside the container. Normally the container contains a certain amount of buffer electrolyte when the measurement starts. Samples are then added by pipetting. The fluidic convection in the small container is driven by the released surface energy from the droplet [97] and the convection speed can reach 0.15 m/s for the container used in our experiments. Therefore, the mixing is fast and the sample becomes evenly distributed in the container within seconds. The response time of the sensor is limited by surface reaction when the sample concentration is high. With low sample concentration, the sensor response time is determined by the transportation of molecules or ions through the depletion zone above the sensor surface, whose thickness δ_s increases with time t, *i.e.*, $\delta_s = \sqrt{Dt}$, where D is the diffusivity [45]. It is worth noting that the transport of biomolecules or ions through the 5 mm distance from the top to the bottom of the container is actually driven by convection, not by diffusion, which is proven by the fast response during ion sensing [69].

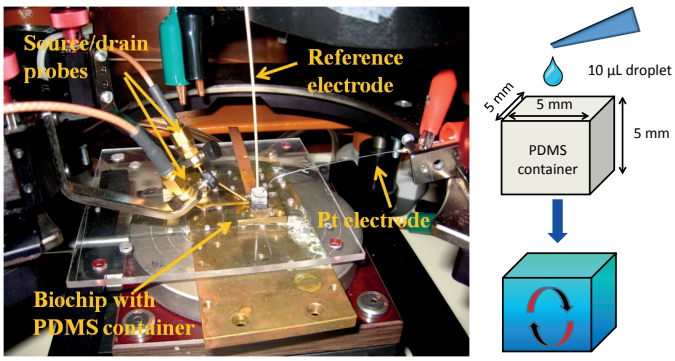

Figure 3.5. Photo picture (left) and schematic representation (right) of sample delivery with a PDMS container. The SiNWFET sensors are located at the bottom of the container.

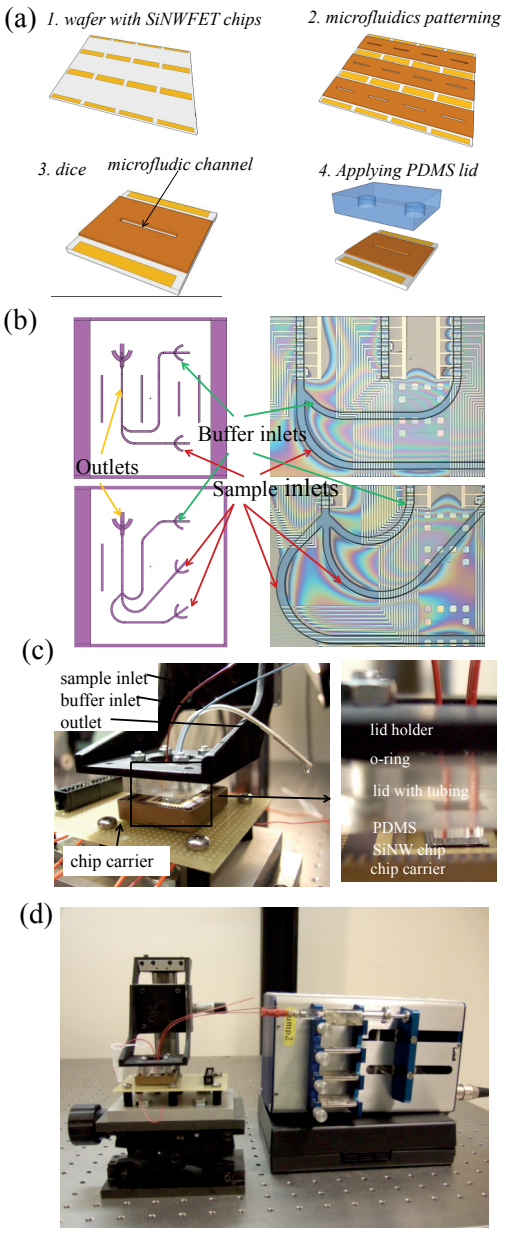

Figure 3.6. (a) Schematic representation of the fabrication process of SU-8 microfluidic channels on SiNWFET chips, (b) layout designs and optical micrographs of the SU-8 channels on the SiNWFET chip, photos of (c) lid for microfluidic channels with inlet and outlet tubes, and (d) chip dock and syringe pump.

3.2.2. The microfluidic system delivery method

An on-chip microfluidic system was developed through collaboration with Acreo AB in Kista-Stockholm, aiming at minimization of sample volume, shorter molecular diffusion length, fast buffer-to-sample switching, and accurate sample delivery to different sensors. The introduction of the laminar flow in the microfluidic channel suppresses the growth of the depletion zone so as to achieve short diffusion length and fast mass transport to the sensor surface [45].

As shown in Figure 3.6(a), after the metallization step, the wafer with SiNWFET chips was spun-coated with an SU-8 layer of 100 μm thickness. SU-8 is an epoxy-based negative photoresist and in our experiment the microfluidic channels were formed by patterning the SU-8 layer with lithography. Figure 3.6(b) shows different designs of microfluidic channels with two or three inlets and their corresponding optical micrographs after fabrication. After the SU-8 curing process, the wafer was diced and the chips were cleaned. As shown in Figure 3.6(c), a position-controlled glass lid was applied on top of the chip with a PDMS sealing layer in between. The tubes in the lid can be manually aligned to the inlet and outlet holes of the microfluidic channels on the chip. The sample was delivered by a syringe pump controlled by a step motor as seen in Figure 3.6(d).

3.3. *p*H sensing with unfunctionalized device

*p*H sensing was carried out on two unfunctionalized FETs with 0.2 μm (nanowire, NW) and 2 μm (microwire, MW) channel widths in order to confirm if the sensors were functioning properly, *i.e.*, if they are sensitive to φ_s variations. The *p*H sensing arrangement is schematically shown in Figure 3.7(a). The Ag/AgCl reference gate electrode was applied to ensure that only $\Delta\varphi_s$ at the gate oxide/electrolyte interface contributed to the signal. Two FETs were biased in the subthreshold region, *i.e.*, V_G=-0.5V, during I_{DS} sampling as shown in Figure 3.7(b). Results showed no significant differences in both normalized ΔI_{DS} ($\Delta I_{DS}/I_{DS0}$, I_{DS0} is the baseline current) and $\Delta\varphi_s$ for the two FETs as shown in Figure 3.7(c) and (d). As mentioned earlier, $\Delta\varphi_s$ only depends on the properties of gate material and electrolyte so it should be the same for both devices. With similar *SS* near the bias point, both FETs should give similar current sensitivities, *i.e.*, I_{DS}/I_{DS0}, as indeed is the case in Figure 3.7.

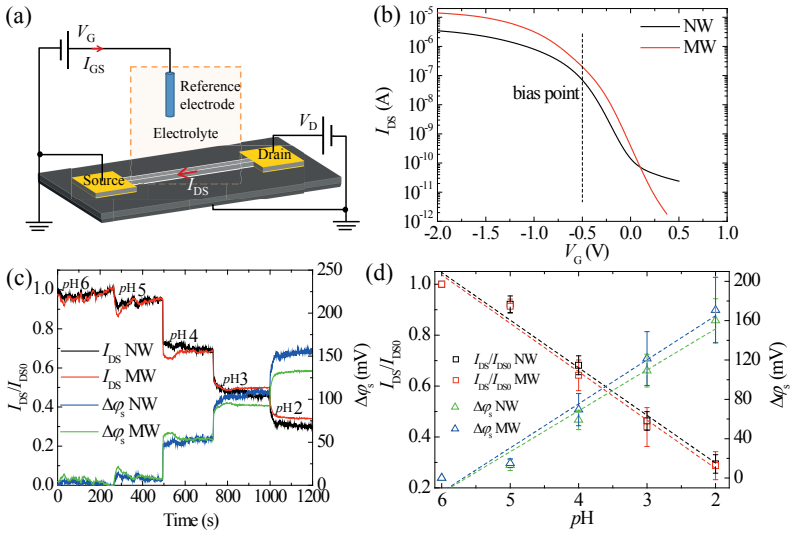

Figure 3.7. (a) Schematic representation of the pH sensing arrangement, (b) Transfer characteristics of two FETs with 0.2 µm (nanowire, NW) and 2 µm (microwire, MW) channel widths, both devices were gated by reference electrode, (c) normalized I_{DS} and $\Delta\varphi_s$ when changing the electrolyte pH from 6 to 2, and (d) summary of pH sensitivities for the two FETs.

3.4. Surface functionalization

Surface functionalization was performed through collaboration with KTH Biotechnology. The detailed process is schematically shown in Figure 3.8. To start with, chips with SiNWFETs were cleaned in an acetone bath with sonication and then treated with O_2 plasma to generate a fresh surface with hydroxyl groups (–OH). The –OH terminated surface was silanized with (3-aminopropyl)triethoxysilane (APTES) to convert the –OH groups to amino groups ($–NH_2$). A further reaction with succinic anhydride converted the $–NH_2$ groups to carboxyl groups (–COOH). Finally, the carboxyl groups reacted with ethyl(dimethylaminopropyl) carbodiimide (EDC) and *N*-hydroxysuccinimide (NHS) for introduction of active NHS-ester, which could react with the primary $–NH_2$ group on the amino acid linker of the receptors thus forming a covalent bond by amide bond. To avoid nonspecific binding, the unreacted sites were blocked by ethanolamine.

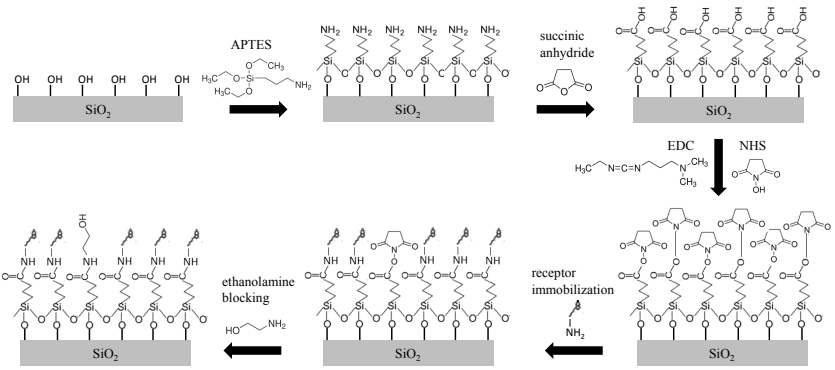

Figure 3.8. Schematic representation of the surface functionalization process with using APTES as an example [98].

One critical step with the functionalization is silanization, *i.e.*, APTES treatment, of the SiO_2 surface terminated with –OH groups [99–103]. An ideal surface after silanization should be covered with a uniform self-assembled monolayer (SAM) with a high density of $–NH_2$ groups. The morphology and thickness of the SAM can be characterized by atomic force microscopy (AFM) and ellipsometry, respectively [100, 101, 103]. The density of $–NH_2$ groups is normally evaluated by examining the surface concentration of nitrogen atoms with X-ray photoelectron spectroscopy (XPS) or surface free energy by contact angle measurement (CAM) [103, 104]. The drawback of using APTES for SAM formation is that the trifunctional reactive groups of APTES are very likely to lead to network formation, causing nonuniformity on the active area of the sensor or growth of thick interfacial layer. The latter can further complicate the definition and function of the Debye screening length. As a result, some researchers have turned to monofunctional silanes such as (3-aminopropyl)dimethylethoxysilane (APDMS) instead of APTES for SAM formation [56, 103]. The density of receptors after immobilization can be estimated by measuring the fluorescence signal from the bound targets conjunct with fluorescence tags such as cy3 or cy5. It is worth noting that the substrate interference effect must be taken into account when comparing fluorescence intensities of samples with different substrate materials or same material of different thicknesses [105]. For applications where multiplex detection is desired, *i.e.*, several target biomolecules need to be identified in one single measurement, different receptors can be immobilized on different SiNWFETs by spotting. In our experiment, the spot size can be limited to about 100 μm in diameter with good control.

3.5. Preliminary protein and ssDNA sensing with PDMS container

Detection of proteins and ssDNA was performed with SiNWFETs after the functionalization process. A PDMS container was used for sample delivery as shown in Figure 3.5. When the measurements started, the container was filled with 90 µL of buffer electrolyte, *i.e.*, 0.1X phosphate buffered saline (PBS). After the stabilization of the I_{DS} baseline, 10 µL of sample electrolyte containing the biomolecules was added into the container. The sample and starting buffer electrolytes should have exactly the same ionic concentration and *p*H value in order to avoid the bulk effect, *i.e.*, false response as a result of change in *p*H or ionic strength in the electrolyte. Protein detection experiments with an Affibody model system were carried out on a SiNWFET functionalized with anti-Taq Affibody, *i.e.*, Ztaq [66]. The *p*H value of the electrolyte was 7.4 so both Zztaq (*p*I=8.3) and Zztaq Lys-tail (*p*I=9.9) were positively charged while Zztaq Glu-tail (*p*I=4.9) was negatively charged. As shown in Figure 3.9(a), I_{DS} of the SiNWFET with hole conduction decreases when Zztaq or Zztaq Lys-tail is added, while in contrary it increases when Zztaq Glu-tail is added. The concentrations shown in the figure are the final concentrations in the container after the addition. A control experiment was

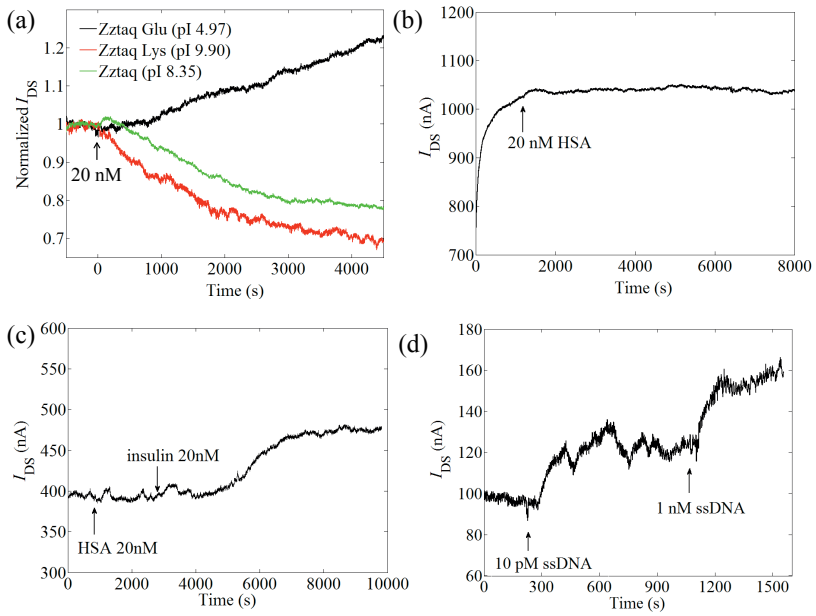

Figure 3.9. (a) Real-time detection of Zztaq, Zztaq Glu, and Zztaq Lys (20 nM each) with different pI values in a PBS buffer (pH=7.4) by a Ztaq-functionalized SiNWFET. (b) Control experiment with 20 nM HSA. Detection of (c) insulin and (d) ssDNA with Zinsulin and ssDNA functionalized SiNWFETs, respectively.

also performed on the same device with human serum albumin (HSA) and no response was observed in 2 hours after the injection as seen in Figure 3.9(b). The experimental results demonstrate that the Ztaq-functionalized SiNWFET can indeed selectively detect Zztaq Affibody molecules and the direction of I_{DS} changes depend on the charge polarity of the protein as well as the carrier type of the SiNWFET [46]. Meanwhile, an insulin detection experiment was performed on a SiNWFET functionalized with the anti-insulin Affibody Zinsulin. As shown in Figure 3.9(c), the I_{DS} remained unchanged after the injection of HSA (control sample) while it increased after the injection of 20 nM negatively charged insulin (pI=5.3) [106]. Furthermore, hybridization of complementary ssDNA with negatively charged backbone led to an I_{DS} increase as shown in Figure 3.9(d) [56, 62, 96, 107].

Although the initial experimental results were encouraging, further studies, such as comparison of antibody and Affibody receptors and optimization of device parameters, were greatly hindered by the poor reproducibility. The detection signal varied significantly from batch to batch and some devices even showed no responses to the target biomolecules. Meanwhile, no clear dependence of current response on sample concentration was obtained, and the detection with microfluidics remained unsuccessful. Possible causes could be a poor control of the surface functionalization which led to a non-uniform SAM layer and receptor density on the active area of the sensor.

3.6. *C-V* and *I-V* characterization on graphene-based field-effect transistor

The setup for *C-V* and *I-V* characterization of graphene-based field-effect transistor is schematically shown in Figure 3.10(a). The *C-V* measurement was performed using an HP4284A LCR meter and with a three-electrode electrochemical configuration [73]. An AC current (I_M, 100 Hz) and a DC bias were applied between a Pt counter electrode (CE) and the source/drain electrode of the graphene sensor device. Both AC (V_M) and DC (V_G vs. a reference potential) potential drops across the graphene/electrolyte interface were recorded by the Ag/AgCl reference electrode (RE). The impedance (Z) of the interface is equal to V_M/I_M and C_G of the sensor is calculated as $C_G = \frac{1}{2\pi f Z''}$, where f is frequency in Hz and Z'' is the imaginary part of Z. During the *I-V* characterization, V_G was applied to RE inserted in the electrolyte in order to achieve a stable electrolyte potential.

However, I_{DS} of the graphene-based FET operating in electrolyte often took several seconds to become stabilized as shown in Figure 3.10(b). This instability is probably due to the charging of the graphene/electrolyte interface. Figure 3.10(c) shows the transfer characteristics of the graphene transistor measured at different NaCl solutions with 0 s measurement delay, *i.e.*,

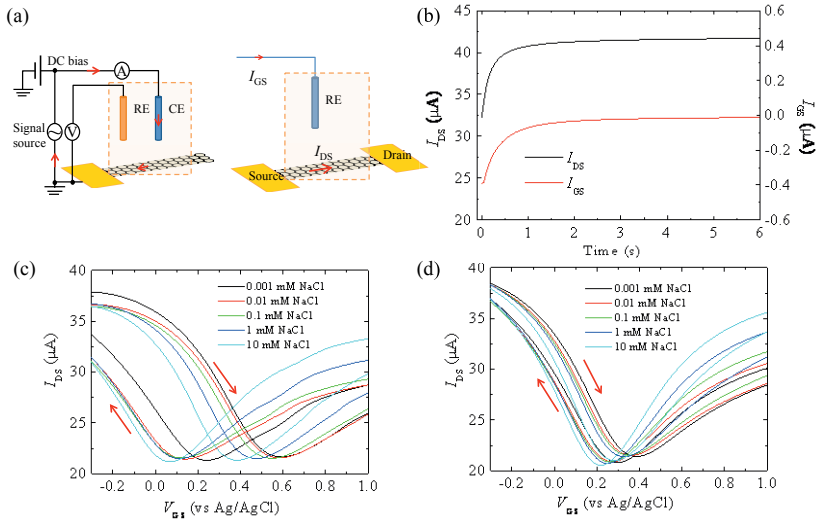

Figure 3.10. (a) Schematic representations of the C-V (left) and I-V (right) measurement arrangements. RE: Ag/AgCl reference electrode, CE: Pt counter electrode; (b) I_{DS} and I_{GS} as a function of time for the graphene transistor operating in electrolyte with V_G=-0.5 V; I-V characteristics and hysteresis behavior observed when conducting the measurements in electrolyte of different NaCl concentrations with a delay of (b) 0 s and (c) 2 s from the time point of applying the voltage to that of reading the current.

I_{DS} was read right after applying V_G. Large hysteresis could be observed and $\Delta\varphi_s$ obtained by correlating to the *I-V* curve shift as a result of Na^+ adsorption strongly depended on the sweeping direction. This distortion can be significantly reduced by increasing the measurement delay time, as shown in Figure 3.10(d).

3.7. Electrical characterization and multiplex sensing platform

Prior to the fabrication of microfluidic channels, the I_{DS}-V_G measurement was always performed on the SiNWFETs at room temperature on a probe-station with an HP4156A precision semiconductor parameter analyzer. To assess the sensing performance of the SiNWFETs with high flexibility, a characterization system combining a Keithley KE6487 to source V_G and sense I_G and a Keithley KE2636A to source V_{DS} and sense I_{DS} has been built. The system can perform both sweep and sampling measurements. It is further expanded so it can simultaneously monitor the metallic gate electrode/electrolyte interfacial potential (φ_{ME} as shown in Figure 2.1(c)) and I_{DS}. With this capability, the stability of φ_{ME} in the presence of an electrolyte

with unstable redox potential can be studied. For current sampling measurements, the SiNWFET is biased in the subthreshold region where the device is most sensitive to $\Delta\varphi_s$ because of the exponential dependence of I_{DS} on φ_s [51, 57]. The instruments were controlled by home-made LabView programs.

A multiplex detection platform has also been developed in order to enable simultaneous monitoring of several SiNWFETs functionalized with different receptors. The switching function is carried out by an HP3488A switch unit. For transfer characteristics measurement, *i.e.*, I_{DS} vs V_G, all SiNWFETs share the same V_{GS} source (KE6487) while the V_{DS} source (channel B of KE2636A) is sequentially connected to the drain terminals of the SiNWFETs. As shown in Figure 3.11(a) as an example, when a measurement starts, terminals b0 and n0 are connected and the I_{DS} vs V_G measurement is performed on NW0. After the measurement, b0 and n0 are disconnected and then b1 and n1 are connected for measurement on NW1. The I_{DS} *vs.* V_G measurement is halted when the measurements on all 5 SiNWFETs are accomplished.

For current sampling measurement, a common V_{GS} source is used to bias all SiNWFETs in the subthreshold region. A constant bias, *e.g.*, +1 V, is

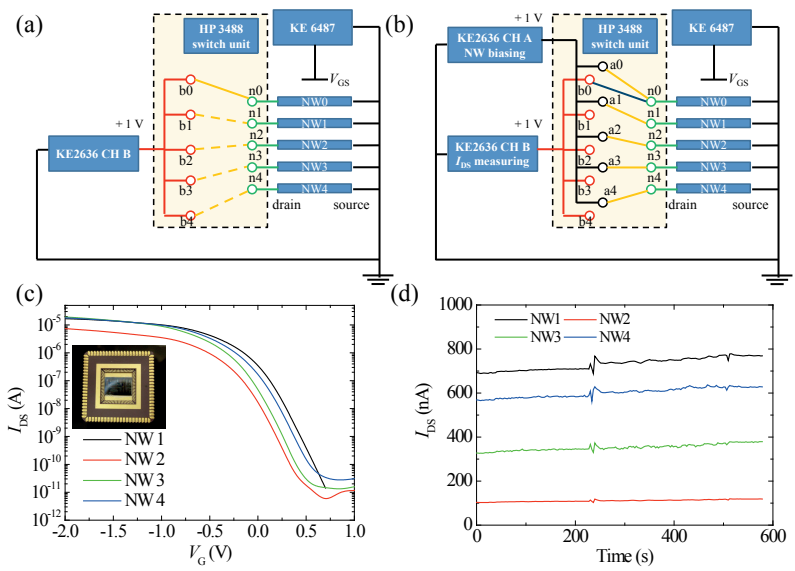

Figure 3.11. Schematic representations of multiplex measurement designs for (a) IV sweep and (b) current sampling, and the corresponding test measurement results for 4 SiNWFETs, i.e., (c) I_{DS} vs V_G and (d) I_{DS} vs time. Insert in (c): a photo picture of a test chip after wire bonding.

applied to the drain terminals of all SiNWFETs through channel A of KE2636A. The I_{DS} measurement of each SiNWFET is performed at channel B of KE2636A. In detail, when a measurement starts, the drain terminals of all SiNWFETs are first connected to channel A of KE2636A, *i.e.*, the biasing channel. To sample I_{DS} of NW0, n0 was disconnected from a0 (the biasing channel) but connected to b0 (the measuring channel). After the sampling, n0 is disconnected from b0 and reconnected to a0. The same procedure is applied to all devices. The drain terminals of all SiNWFETs are under constant bias during the entire measurement except for the switching period. The time needed for a single switch action is about 10 ms. It is essential to maintain a constant bias to the SiNWFETs throughout the sampling measurement because the stabilization of the devices takes about 15 min due to the I_{DS} transient and drift caused by the slow movement of ions in an electrolyte under an electrical field [59]. Upon removal of the electrical field when finishing one sampling point, the ions have a tendency to return to their original positions. The relaxation of ions could affect the measurement accuracy of next sampling point, especially if the unbiased period of the SiNWFET is long. The design schematically shown in Figure 3.11(b) is aimed at minimization of the unbiased period for SiNWFETs during the sampling measurement.

4. Overview of the Appended Papers

Paper I is mainly focused on the fabrication and passivation of SiNWFETs. Since the back-gate is the simplest gate configuration and has been widely used in biosensor applications [25, 46, 108, 109], extensive efforts have been devoted to understanding of the gate coupling efficiency and carrier distributions of back-gated SiNWFETs. It could be emphasized that different from the vast majority of published device fabrication schemes, a unique yet CMOS-process compatible fabrication process is presented in this paper. A detailed description of the top-down fabrication process as well as the RTO passivation can be found in the experimental method section of **Paper I**.

The transfer characteristics of the SiNWFET measured in electrolyte exhibit significantly higher I_{on} and steeper *SS* than measured in air. Finite element analysis shows that C_G of the back-gate SiNWFET operating in electrolyte (ε_r~80) is significantly higher than C_G of the same device operating in air (ε_r=1). When covered by a conductive medium or medium of high ε_r, *e.g.*, electrolyte, the back-gate SiNWFET can be simplified as a double-gate device and its C_G can be viewed as a weighed sum of the bottom gate capacitance (C_{BG}) and top gate capacitance (C_{TG}). Equivalent circuits are used to analyze the back gate coupling to the bottom and top interfaces of a SiNW channel. It was found that C_{TG} of SiNWFET is determined by the thickness of the gate oxide covering the top and sidewall surfaces of the SiNW. Apparently, C_{TG} is significantly higher than C_{BG} because the buried oxide is about 30 times thicker than the gate oxide. However, when operating in air, the gate coupling to the top and sidewall interfaces of the SiNW is negligible and therefore C_G coincides with C_{BG}. It is therefore concluded that the higher I_{on} and steeper *SS* of the SiNWFET result from the enhanced gate coupling to the top and sidewall interfaces of the SiNW due to the presence of the high ε_r medium. It is of particular importance that, when operating in electrolyte, the current conduction along the top and sidewall interfaces dominates even for devices with a back-gate configuration. As a result, these interfaces should be carefully protected during the fabrication process.

The theoretical analysis continues in **Paper II** in which a detailed comparison of gate coupling efficiencies for a SiNWFET with different C_{eox} is found. In an attempt with a more systematic nomenclature in **Paper II**, the back-gate can be categorized as a capacitively-coupled gate, of which the electrical potential of the electrolyte (ψ_{EL}) is equal to the applied back gate voltage (V_{BG}), because of the large substrate area and large C_{sub} as shown in

Figure 4.1(c). For a more generic capacitive gate coupling as shown in Figure 4.1(d), where the gate electrode is placed on the top surface of the chip but insulated by dielectrics such as oxide, ψ_{EL} is jointly determined by the capacitances of the oxide on the gate electrode (C_{eox}), the oxide on the SiNW (C_{tox}), and C_{sub}. The EDL capacitances in the circuits, *i.e.*, C_{DLe}, C_{DLt}, and C_{DLs} are ignored since they are more than 50 times larger than C_{eox}, C_{tox}, and C_{sub}, respectively. With a higher C_{eox}, ψ_{EL} will be closer to V_{BG} and a higher gate coupling efficiency can be expected. Detailed comparison of gate coupling efficiencies for a SiNWFET with different C_{eox} can be found in **Paper II**.

Despite its simplicity, a SiNWFET with a capacitively coupled gate has been shown to be vulnerable to external disturbances. As shown in Figure 4.1(c) and (d), V_G and ground are the known potentials capacitively coupled to the electrolyte. However, unknown external potentials can also be coupled to the electrolyte, *e.g.*, through fluidic delivery systems. Hence, the electrolyte potential becomes unstable and susceptible to external perturbations, as reflected by the noisy I_{DS} and spikes induced by sample additions. In order to reduce perturbations resulting from external electrical fields, a proper shielding of the system is essential. Furthermore, increasing the capacitance between the gate electrode and the electrolyte can also be an effective and practical way to stabilize the electrolyte potential.

One could naturally think of using direct electrical contact with an inert-

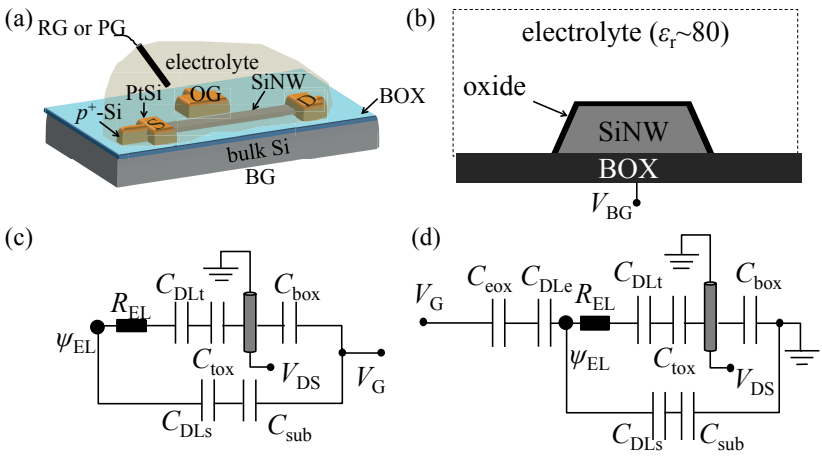

Figure 4.1. (a) Three-dimensional sketch of a SiNWFET covered by electrolyte. RG, PG, BG, and OG represent reference gate, platinum gate, back gate, and top metallic gate covered by oxide, respectively. (b) Cross-section view of a SiNW covered by electrolyte and equivalent small-signal circuit models for a SiNWFET with (c) BG and (d) OG.

metal gate electrode, *e.g.*, Pt or Au, to achieve a stable ψ_{EL} during the measurement. An advantage is that an inert-metal electrode can be easily integrated with the top-down fabrication process. As carefully demonstrated in **Paper III**, the inert-metal/electrolyte contact is unfortunately far from an ideal ohmic contact. The junction potential of the metal/electrolyte contact, *i.e.*, φ_{ME}, as shown in Figure 2.1(b), depends sensitively on the electrochemical equilibrium of the species involved in the electrode reaction [55, 61]. For example, when using Pt as the gate electrode, reactions of redox couples in the electrolyte as well as Pt oxidation can take place at the Pt gate electrode/electrolyte interface [55, 61, 110, 111]. As a result, the φ_{ME} of the Pt/electrolyte contact depends on the [oxidant]/[reductant] ratio as well as $[H^+]$ in the electrolyte. This is demonstrated in **Paper II** by monitoring the response of a Pt-gated SiNWFET when changing the $Fe(CN)_6^{3-}/Fe(CN)_6^{4-}$ ratio and the *p*H value in the electrolyte. In addition, the potential shifts at the Pt/electrolyte and electrolyte/gate insulator interfaces, *i.e.*, $\Delta\varphi_{ME}$ and $\Delta\varphi_s$, jointly contribute to the *p*H response, *i.e.*, ΔV_{TH}, of the Pt-gated SiNWFET.

One should be aware of that the reactivity of "inert" metals in electrolyte could lead to interpretation of fake signals as real responses. To conclude, inert metals are inappropriate candidates as a contacting gate electrode in biosensor applications because they are sensitive to variations of redox potential and *p*H level in the electrolyte. As discussed earlier, a true reference electrode such as Ag/AgCl can be used to fix ψ_{EL} because it has a well-defined electrode reaction and its φ_{ME} is inert to compositional variations in the measurement electrolyte. In **Papers II** and **III**, SiNWFETs gated by a reference gate electrode show no response to changes of the $Fe(CN)_6^{3-}/Fe(CN)_6^{4-}$ ratio in electrolyte, which shows that φ_{ME} of reference gate electrode is not affected by the redox potential in the electrolyte. Further experiments show that the *p*H sensitivities of SiNWFETs with capacitively coupled gate and reference gate are similar. However, for capacitive coupling, changes of φ_s on the oxide covered gate electrode have an opposite polarity to, and hence may cancel out, the change of φ_s at the oxide/electrolyte interface during *p*H sensing.

The response of a SiNWFET to *p*H changes can be interpreted as two separated parts. The first is due to $\Delta\varphi_s$ which only depends on the properties of the gate insulator material and electrolyte. For sensors with the same gate insulator material, their $\Delta\varphi_s$ corresponding to the same *p*H changes should be identical, independent of the dimensions and doping level of the SiNW channel. The second is the relative current change, *i.e.*, $\Delta I_{DS}/I_{DS}$, of the underlying SiNWFET in response to $\Delta\varphi_s$. According to Eqns. (2.4) and (2.5), when the SiNWFET is biased in the subthreshold region and with a small $\Delta\varphi_s$, the relative current change of the SiNWFET in response to $\Delta\varphi_s$ can be derived [112]:

$$\frac{\partial I_{DS}}{I_{DS}\partial \varphi_s} = 2.3SS^{-1}. \quad (4.1)$$

Clearly, the SiNWFET with a smaller *SS* value, *i.e.*, a steeper subthreshold slope, exhibits a higher current sensitivity in response to $\Delta\varphi_s$. The *SS* of a MOSFET is:

$$SS = \frac{dV_G}{d(\log_{10} I_D)} = 2.3\frac{kT}{q}(1 + \frac{C_D + C_{it}}{C_G}), \quad (4.2)$$

where C_D and C_{it} are the depletion capacitance in the channel and the interface state capacitance, respectively [51, 52]. To achieve a low *SS* and high current sensitivity of the SiNWFET, one can consider increasing C_G by reducing the thickness of the gate insulator or using high-κ gate materials. Meanwhile, a lower doping level in the SiNW channel also leads to lower C_D and *SS* and thus higher current sensitivity [50].

The observations in **Paper I** that the top gate as well as the two side gates of a SiNWFET play a more important part than the bottom gate lead to the conception of the two-terminal, self-gating field-effect sensor structure in **Paper IV**. Indeed, we have succeeded in demonstrating that field-effect sensing can be performed even without the gate terminal. In this case, the electrolyte covering the SiNWFET acts as a floating gate and its potential is determined by the potential of the drain terminal V_{DS} (with the source termi-

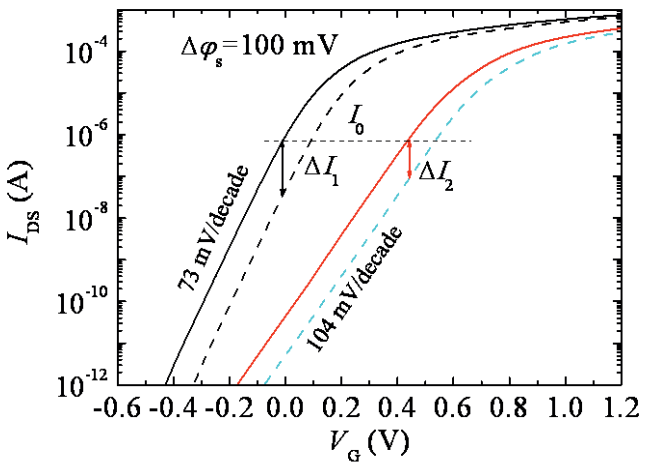

Figure 4.2. Example showing the relationship between current sensitivity and the SS value of SiNWFETs. The SiNWFETs show the same ΔV_{TH} as a result of the surface potential shift ($\Delta\varphi_s$) but the one with a steeper SS gives rise to a higher current sensitivity($\Delta I_1/ I_0 > \Delta I_2/ I_0$).

nal grounded) because of the high dielectric constant of electrolyte. As a result, it is possible to modulate the channel conductance of the SiNWFET by changing the V_{DS}. The two-terminal SiNWFET shows a comparable current sensitivity to *p*H changes to a similarly designed three-terminal SiNWFET. The chief advantage of the two-terminal operation without needing an independent gate electrode is its great simplicity with only two electrodes, thus presenting an opportunity to simplify the chip layout design, chip processing, and measurement system. A challenge is that it is difficult to find the optimized bias point in order to achieve the highest current sensitivity when the SiNWFET is operating in the two-terminal mode. Moreover, the quantification of the sensor response, *i.e.*, extraction of $\Delta\varphi_s$ from ΔI_{DS}, for the two-terminal device is more complex since the transconductance of the working point is difficult to determine.

The drift behavior of SiNWFET with conducting gate electrodes is investigated in **Paper III**. For biosensing experiment especially with low sample concentrations, the signal may take minutes or even hours to reach saturation, see Figure 3.9(a). Under such circumstances, the slow current drift may seriously affect the interpretation of the binding signal. At constant temperature, the current drift of SiNWFETs is mainly due to a slow exchange and subsequent movement of charged species taking place at the gate electrode/electrolyte and electrolyte/oxide interfaces. With Pt as the gate electrode and PBS as the electrolyte, the stabilization of φ_{ME} at the Pt/PBS interface is shown to take about 1000 s due to the low exchange current density of the electrode reaction [59]. Moreover, φ_s at the oxide/electrolyte interface

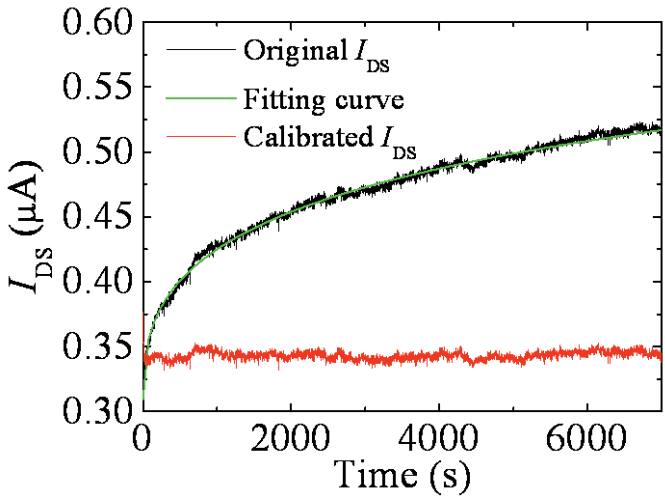

Figure 4.3. Original I_{DS} with drift, curve fitting with stretched-exponential function, and the baseline I_{DS} after calibration for a reference-electrode gated SiNWFET.

also drifts with time because of the reaction of the buried –OH sites [113]. The drift behavior of φ_s can be well described by a stretched-exponential function [114, 115]. The I_{DS} drift of Pt gated SiNWFET is difficult to calibrate because it is jointly determined by the drifts of φ_{ME} and φ_s that are governed by different mechanisms. For reference gated SiNWFET, φ_{ME} is a constant and the I_{DS} drift can only be related to the drift of φ_s which can be readily calibrated as shown in Figure 4.3.

A limitation with SiNWFETs as a sensor working in electrolyte is the difficulty in simultaneously determining the variations of φ_s and C_d at the oxide/electrolyte interface since C_d and C_{ox} are in series connection and C_d is much larger than C_{ox}. A graphene-based field-effect capacitor sensor is demonstrated in **Paper V** to be able to break this barrier. Using basically the same sensor device as schematically shown in Figure 3.10(a), both transistor and capacitor operations are characterized in this paper and the capacitor mode is found to be advantageous since it yields more information than its transistor counterpart. Specifically, the capacitor-mode operation of the sensor device could, in principle, facilitate the extraction of the density of bound biomolecules, which is usually difficult to achieve by measuring $\Delta\varphi_s$ using ISFET. As C_d only depends on the dielectric constant of the bound biomolecules, the capacitor sensor can also detect uncharged molecules. Furthermore, the graphene capacitor sensor is shown to be capable of tracking the molecule binding-adsorption kinetics in real-time by monitoring the capacitance transient.

5. Summary and Outlook

In my research leading to the summary of this thesis, a multiplex biomolecular sensing platform with integrated microfluidic system has been developed. The sensors are ISFETs featuring silicon nanowires fabricated using the top-down process. The major focus of this thesis is the operation mechanism of SiNWFETs in electrolyte. For this purpose, different gate configurations are investigated with the assistance of a *p*H sensing model system and small-signal equivalent circuits as well as the well-controllable $Fe(CN)_6^{3-}$/$Fe(CN)_6^{4-}$ redox couple. The major findings of this thesis are summarized below:

1. SiNWFETs were produced through CMOS-compatible top-down process. A SiNW channel with smooth edge profile and small width (<100 nm) was achieved by means of anisotropic wet etching using TMAH. Rapid thermal oxidation was used to grow a thin oxide layer for simultaneous passivation and electrical isolation of the SiNW channel as well as the PtSi source/drain electrodes. Experimental and numerical simulation results showed that the top and sidewall surfaces of the SiNW channel were the main current conduction paths when the devices were operating in electrolyte, irrespective of gate configurations. As a result, a smooth edge profile of the SiNW is essential to achieve high device performance.

2. Both contacting and insulated electrodes can be used as the gate electrode for the SiNWFETs. It is essential for the contacting electrodes to have well-defined electrode reactions and stable electrode potentials during biosensing experiments. Inert metals, such as Pt, are, however, sensitive to the redox potential and *p*H level in the electrolyte and thus may lead to a false response to undesired disturbances such as unavoidable *p*H variations. For insulated gate electrodes with capacitive coupling, the gate coupling efficiency can be improved by increasing the capacitance between the gate electrode and the electrolyte. Although the SiNWFETs with contacting and insulated electrodes showed comparable *p*H sensitivity, devices with insulated gate electrodes were more vulnerable to external disturbances.

3. In consistency with point 1 above, field-effect sensing can also be performed without a gate electrode. The electrolyte covering the SiNWFET can in fact act as a floating gate and its potential is determined by the potential of the drain terminal. Thus the conductance of the SiNW channel can be modulated by V_{DS}. A drawback with this device configuration is that it is difficult to optimize the bias point and quantify the response.

4. The drift of φ_{ME} at the Pt/PBS interface and that of φ_s at the oxide/electrolyte interface jointly contribute to the I_{DS} drift of Pt-gated SiNWFETs. The I_{DS} drift of a reference-electrode gated SiNWFET only depends on φ_s drift. Hence it can be well described by a stretched-exponential function and readily calibrated.

5. Protein detection using Affibody molecules as receptors was performed. The sensors could selectively detect the target proteins and the directionality of the I_{DS} changes was in good agreement with the charge polarities of the proteins. However, a systematic comparison of Affibody and antibody receptors would require a better reproducibility of the detection signal. A better control of surface functionalization leading to a uniform SAM layer and receptor density on the active area of the sensor is essential.

6. The field-effect detection was extended to using a graphene capacitor in order to explore the possibility of simultaneously determining the variations of φ_s and C_d at graphene/electrolyte interface. In addition, the graphene capacitor sensor was shown to be capable of tracking the molecule binding-adsorption kinetics in real-time by monitoring the capacitance transient.

To achieve the ultimate goal of ultra-sensitive detection of biomolecules, much more needs to be done so as to optimize the surface functionalization process and device geometry. At the same time, improvement of the sensitivity and signal-to-noise ratio of ISFET based *p*H sensors is extremely important in many applications. Some of the needed efforts are suggested as follows:

1. Pt could be used as gate electrode for easier integration purpose if a *p*H insensitive reference device is included. The instability of Pt electrode can be sensed by the reference device and thus be calibrated.

2. Materials with higher β_{int} such as Ta_2O_5 and Al_2O_3 could be used to replace SiO_2 as the gate insulator in order to increase the *p*H sensitivity ($\Delta\varphi_s/\Delta p$H).

3. The geometry and doping level of the channel region of the sensor should be optimized to achieve a steeper *SS* and thus higher current sensitivity to $\Delta\varphi_s$.

4. The research on graphene-based field-effect sensors is in its early stage. The possibility of carrying on multi-principle detections, *e.g.* electronic (capacitor and transistor), electrochemical, etc., needs further exploration.

Finally, the recent commercial success of the Ion Torrent technology for semiconductor genome sequencing [35] demonstrates how the almighty silicon technology can profoundly impact the healthcare sector with an entirely new product. Ion Torrent has indeed been rapidly developing their chip technology by benefitting from the well-developed silicon microfabrication technology. One prerequisite for success is that the chip fabrication can utilize semiconductor foundries which provide standard processing for competitive prices. High-density sensor chips are indispensable for high-speed, high-accuracy, and low-cost genome sequencing. The great potential of the

silicon-based semiconductor sequencing technology also lies in the natural integration of various (standard) circuitries for signal processing and transmission. However, the depth of penetration of the semiconductor genome sequencing technology in the healthcare sector will partly and heavily depend on how the specific chip technology can fully exploit the already achieved aggressive downscaling of CMOS technology in pace with Moore's Law [116].

Sammanfattning på svenska

Point-of-care (POC)-diagnostik möjliggör en ny gigantisk marknad, som kan komma att påverka vår vardag i grunden. Mer specifikt så kan detektion av DNA och proteiner komma att bli startpunkten vid diagnos av många olika sjukdomar, t.ex. cancer, hjärt- och kärlsjukdomar, olika infektioner och allergier. För att kunna hitta markörer för dessa sjukdomar med dagens teknik så krävs det mycket labbarbete och det blir därmed både dyrt och tidskrävande. De metoder som används är oftast baserade på optisk upptäck och igenkänning. Dessa metoder har inte särskilt bra specificitet eller sensitivtet, de måste kollas manuellt och testerna kan inte köras parallellt utan anställa fler läkare vilket gör testerna dyra.

Det har rappporterats att elektroniska sensorer baserade på fälteffekttransistorer av kiselnanotrådar (SiNWFET) kan upptäcka biomolekyler vid så låga koncentrationer so fM med mycket hög specificitet. Även om dessa rapporter ännu inte är fullt bekräftade så är deras tillverkningsprocess en mycket stor fördel. Den är helt CMOS-kompatibel och möjliggör därmed produktion med hög densitet av enheter och en mycket låg tillverkningskostnad, två egenskaper som är av yttersta vikt för att POC ska bli verklighet. Idén om en fäteffektssensor introducerades av Bergveld under tidigt 1970-tal när han presenterade sin jonkänsliga fälteffektstransstor (ISFET). En ISFET är mycket lik en MOSFET med skillnaden att den jonkänsliga varianten har gaten skild från chipet. Den har istället en referenselektrod i en elektrolyt där elektrolyten har direktkontakt med gate-isoleringen. När ISFET-ens gateisolering är i kontakt med elektrolyten så bildas ett så kallat elektriskt dubbellager (EDL) vid ytan mellan isoleringen och elektrolyten. Det bildas en spänning (φ_s) över dubbellagret och denna spänning är en funktion av isolatorytans ytladdningsdensitet (σ_s) och differentialkapacitansen (C_d) hos EDL, $\varphi_s=\sigma_s/C_d$. Ytreaktioner eller biomolekyler som bnder till isolatorytn kommer att leda till förändringar av både σ_s och φ_s som kan upptäckas genom att mäta skillnaden i tröskelspänning för ISFET-en (ΔV_{TH}).

Den här avhandlingen fokuserar på utvecklingen av en multiplex mätplattform baserad på SiNWFET integrerat med ett mikrofluidikssytem som ska föra fram proverna till sensorn. Mycket arbete har lagts ned på att ta fram en top-down process för tillverkning av sensorerna samt en effektiv passivering av dessa. Olika gate-konfigurationer studerades experimentellt med stöd av numeriska beräkningar och kretsscheman för att ta reda på hur de fungerar samt deras styrningseffektivitet. Ph-mätningar användes som ett

modellsystem och mycket arbete lades ner på att genom dessa mätningar finna källor som gav upphov till falska mätutslag

Det utvecklades en kalibreringsmodell för att handera att signalen driver iväg under mätningarna. Utöver det så genomfördes proteinmätningsexperiment med små Affibody-molekyler som receptorer på gate-isoleringen för att komma runt problemet med Debye-avskärmning. De viktigaste punkterna i denna avhandling är summerade nedan:

SiNWFET-erna tillverkades genom en CMOS-kompatibel top-downprocess. Kiselnanotrådskanalen (SiNW) med rundad kant och liten bredd ((<100 nm) åstadkoms genom anisotropisk våtetsning med TMAH. Ett tunt lager oxid växtes genom snabb termisk oxidering för att både kemiskt passivera och elektriskt isolera nåde nanotrådskanalen såväl som source/drain-elektroderna av PtSi. Experiment och simuleringar visade att överdelen och sidväggarna av SiNW var de huvudsakliga elektriska ledningsvägarna när sensorn användes i elektrolyt oavsett vilken typ av gate som användes. Därför är det viktigt med en rundad kant för att få välfungerande komponenter.

Både elektroder i direktkontakt med elektrolyten och isolerade elektroder kan användas som gate för SiNWFET. Det är nödvändigt att kontakterande elektroder har väldefinierade reaktioner och en stabil potential under biosensorexperiment. Inerta metaller som t.ex. Pt är tyvärr känsliga för redoxpotentialen och *p*H-värdet i elektrolyten och kan därför ge upphov till falska signaler.

Fälteffektsmätningar kan också utföras utan en gate-elektrod. Elektrolyten ovanför sensorn fungerar d som en flytande gate och dess ptential bestäms av drainterminalen. Konduktansen i SiNW-kanalen bestäms då av V_{DS}. En nackdel med den här uppställningen är att det är svårt att hitta en optimal arbetspotential och att kvantifiera den resulterande signalen.

Att spänningen φ_{ME} över gränsytan mellan Pt och PBS och att spänningen φ_s över oxid/elektrolyt-gränsytan driver bidrar båda till att strömmen I_{DS} driver vid mätningar med en Pt-gate. Om I_{DS} driver vid mätningar med en referenselektrod så beror det enbart på att spänningen φ_s driver. Den effekten kan beskrivas med en utdragen exponentialfunktion och kalibreras.

Proteinmätningar med Affibody-molekyler utfördes. Sensorn kunde selektivt upptäcka målproteinerna och riktningen på förändringen av I_{DS} stämde väl överens med laddningen på proteinerna. För att kunna göra en systematisk jämförelse mellan receptorer med Affibody-molekyler och de med antikroppar skulle det behövas en mer upprepningsbar mätprocedur. Bättre kontroll över ytfunktionaliseringen som ska ge ett uniformt monolager och bättre kontroll över receptordensiteten är av yttersta vikt.

En begränsning som SiNWFET har när den används som jonsensor i elektrolyt är att det är svårt att samtidigt bestämma hur φ_s och C_d vid gränsytan mellan oxid och elektrolyt varierar när jonkoncentrationen ändras. Detta beror på att oxidlagrets kapacitans C_{ox} är mycket större än C_d och eftersom

dessa kapacitanser är seriekopplade så blir skillnader i C_d svåra att läsa av. Det har demonstrerats att en grafenbaserad fälteffektkapacitator kan fungera bättre som sensor då den inte behöver ha ett oxidlager. En sådan sensor som arbetar i kapacitansläge skulle, i princip, möjliggöra mätningar av densiteten av bundna biomolekyler, något som är mycket svårt att göra genom att mäta $\Delta\varphi_s$ med en ISFET. Eftersom C_d enbart beror på den dielektriska konstanten hos lagret av bundna biomolekyler så skulle en kapacintanssensor kunna mäta oladdade molekyler. Dessutom visas det att en grafenkapacitanssensor klarar av att mäta molekylbindningskinetiken i realtid genom att läsa av den transienta kapacitansen.

References

[1] W. Lutz, W. Sanderson, and S. Scherbov, "The coming acceleration of global population ageing," *Nature*, vol. 451, pp. 716–9, 2008.

[2] V. Gubala, L. F. Harris, A. J. Ricco, M. X. Tan, and D. E. Williams, "Point of care diagnostics: status and future," *Analytical Chemistry*, vol. 84, pp. 487–515, 2012.

[3] A. Warsinke, "Point-of-care testing of proteins," *Analytical and Bioanalytical Chemistry*, vol. 393, pp. 1393–405, 2009.

[4] P. B. Luppa, C. Müller, A. Schlichtiger, and H. Schlebusch, "Point-of-care testing (POCT): Current techniques and future perspectives," *Trends in Analytical Chemistry*, vol. 30, pp. 887–898, 2011.

[5] C. A. Lehmann, *Point-of-Care Testing*. Washington, DC: American Association for Clinical Chemistry Inc., 2004, pp. 269–277.

[6] J. Wang, "Electrochemical glucose biosensors," *Chemical Reviews*, vol. 108, pp. 814–25, 2008.

[7] A. Niemz, T. M. Ferguson, and D. S. Boyle, "Point-of-care nucleic acid testing for infectious diseases," *Trends in Biotechnology*, vol. 29, pp. 240–50, 2011.

[8] R. McNerney and P. Daley, "Towards a point-of-care test for active tuberculosis: obstacles and opportunities," *Nature Reviews Microbiology*, vol. 9, pp. 204–13, 2011.

[9] L. Gervais, N. de Rooij, and E. Delamarche, "Microfluidic chips for point-of-care immunodiagnostics," *Advanced Materials*, vol. 23, pp. H151–76, 2011.

[10] E. T. Carlen and A. van den Berg, "Nanowire electrochemical sensors: can we live without labels?," *Lab Chip*, vol. 7, pp. 19–23, 2007.

[11] C. Boozer, G. Kim, S. Cong, H. Guan, and T. Londergan, "Looking towards label-free biomolecular interaction analysis in a high-throughput format: a review of new surface plasmon resonance technologies," *Current Opinion in Biotechnology*, vol. 17, pp. 400–5, 2006.

[12] M. M.-C. Cheng, G. Cuda, Y. L. Bunimovich, M. Gaspari, J. R. Heath, H. D. Hill, C. A. Mirkin, A. J. Nijdam, R. Terracciano, T. Thundat, and M. Ferrari, "Nanotechnologies for biomolecular detection and medical diagnostics," *Current Opinion in Chemical Biology*, vol. 10, pp. 11–19, 2006.

[13] J. Daniels and N. Pourmand, “Label-free impedance biosensors: opportunities and challenges,” *Electroanalysis*, vol. 19, pp. 1239–1257, 2007.
[14] M.-Y. Wei, S.-D. Wen, X.-Q. Yang, and L.-H. Guo, “Development of redox-labeled electrochemical immunoassay for polycyclic aromatic hydrocarbons with controlled surface modification and catalytic voltammetric detection,” *Biosensors and Bioelectronics*, vol. 24, pp. 2909–14, 2009.
[15] B. S. Gaylord, A. J. Heeger, and G. C. Bazan, “DNA hybridization detection with water-soluble conjugated polymers and chromophore-labeled single-stranded DNA,” *Journal of the American Chemical Society*, vol. 125, pp. 896–900, 2003.
[16] L. Gervais and E. Delamarche, “Toward one-step point-of-care immunodiagnostics using capillary-driven microfluidics and PDMS substrates,” *Lab Chip*, vol. 9, pp. 3330–7, 2009.
[17] N. C. Tansil and Z. Gao, “Nanoparticles in biomolecular detection,” *Nano Today*, vol. 1, pp. 28–37, 2006.
[18] C. Zhang and J. Hu, “Single quantum dot-based nanosensor for multiple DNA detection,” *Analytical Chemistry*, vol. 82, pp. 1921–7, 2010.
[19] H. Jans and Q. Huo, “Gold nanoparticle-enabled biological and chemical detection and analysis,” *Chemical Society Reviews*, vol. 41, pp. 2849–66, 2012.
[20] R. S. Gaster, L. Xu, S.-J. Han, R. J. Wilson, D. A. Hall, S. J. Osterfeld, H. Yu, and S. X. Wang, “Quantification of protein interactions and solution transport using high-density GMR sensor arrays,” *Nature Nanotechnology*, vol. 6, pp. 314–20, 2011.
[21] J. R. L. Ehrenkranz, “Home and point-of-care pregnancy tests : a review of the technology,” *Epidemiology*, vol. 13, pp. S15–18, 2002.
[22] P. Bergveld, “Thirty years of ISFETOLOGY: What happened in the past 30 years and what may happen in the next 30 years,” *Sensors and Actuators B*, vol. 88, pp. 1–20, 2003.
[23] M. J. Schöning and A. Poghossian, “Recent advances in biologically sensitive field-effect transistors (BioFETs),” *Analyst*, vol. 127, pp. 1137–1151, 2002.
[24] P. Bergveld, “ISFET, Theory and Practice,” in *IEEE Sensor Conference*, 2003, October, pp. 1–26.
[25] E. Stern, A. Vacic, C. Li, F. N. Ishikawa, C. Zhou, M. A. Reed, and T. M. Fahmy, “A nanoelectronic enzyme-linked immunosorbent assay for detection of proteins in physiological solutions,” *Small*, vol. 6, pp. 232–8, 2010.
[26] C. K. O’Sullivan and G. G. Guilbault, “Commercial quartz crystal microbalances – theory and applications,” *Biosensors and Bioelectronics*, vol. 14, pp. 663–670, 1999.

[27] R. Hart, E. Ergezen, R. Lec, and H. Noh, “Improved protein detection on an AC electrokinetic quartz crystal microbalance (EKQCM),” *Biosensors and Bioelectronics*, vol. 26, pp. 3391–3397, 2011.
[28] J. Homola, S. Yee, and G. Gauglitz, “Surface plasmon resonance sensors: review,” *Sensors and Actuators B*, vol. 54, pp. 3–15, 1999.
[29] M. Svedendahl, “Comparison of LSPR and SPR biosensors,” 2009.
[30] R. Karlsson, P. S. Katsamba, H. Nordin, E. Pol, and D. G. Myszka, “Analyzing a kinetic titration series using affinity biosensors,” *Analytical Biochemistry*, vol. 349, pp. 136–47, 2006.
[31] P. Bergveld, “Development of an ion-sensitive solid-state device for neurophysiological measurements,” *IEEE Transactions on Bio-Medical Engineering*, vol. BME-17, pp. 70–71, 1970.
[32] S. Chen, J. G. Bomer, E. T. Carlen, and A. van den Berg, “Al_2O_3/silicon nanoISFET with near ideal nernstian response,” *Nano Letters*, vol. 11, pp. 2334–41, 2011.
[33] L. Bousse, N. F. De Rooij, and P. Bergveld, “Operation of chemically sensitive field-effect sensors as a function of the insulator-electrolyte interface,” *IEEE Transactions on Electron Devices*, vol. ED-30, pp. 1263–1270, 1983.
[34] M. Waleed Shinwari, M. Jamal Deen, and D. Landheer, “Study of the electrolyte-insulator-semiconductor field-effect transistor (EISFET) with applications in biosensor design,” *Microelectronics Reliability*, vol. 47, pp. 2025–2057, 2007.
[35] J. M. Rothberg, W. Hinz, T. M. Rearick, J. Schultz, W. Mileski, M. Davey, J. H. Leamon, K. Johnson, M. J. Milgrew, M. Edwards, J. Hoon, J. F. Simons, D. Marran, J. W. Myers, J. F. Davidson, A. Branting, J. R. Nobile, B. P. Puc, D. Light, T. A. Clark, M. Huber, J. T. Branciforte, I. B. Stoner, S. E. Cawley, M. Lyons, Y. Fu, N. Homer, M. Sedova, X. Miao, B. Reed, J. Sabina, E. Feierstein, M. Schorn, M. Alanjary, E. Dimalanta, D. Dressman, R. Kasinskas, T. Sokolsky, J. A. Fidanza, E. Namsaraev, K. J. McKernan, A. Williams, G. T. Roth, and J. Bustillo, “An integrated semiconductor device enabling non-optical genome sequencing,” *Nature*, vol. 475, pp. 348–52, 2011.
[36] P. Bergveld, “A critical evaluation of direct electrical protein detection methods,” *Biosensors and Bioelectronics*, vol. 6, pp. 55–72, 1991.
[37] R. B. M. Schasfoort, P. Bergveld, R. P. H. Kooyman, and J. Greve, “Possibilities and limitations of direct detection of protein charges by means of an immunological field-effect transistor,” *Analytica Chimica Acta*, vol. 238, pp. 323–329, 1990.
[38] P. Bergveld, “The future of biosensors,” *Sensors and Actuators A*, vol. 56, pp. 65–73, 1996.
[39] J. Janata and S. Moss, “Chemically sensitive field-effect transistors,” *Biomedical Engineering*, vol. 11, pp. 241–5, 1976.

[40] J. F. Schenck, *Theory, design and biomedical applications of solid state chemical sensors*. Boca Raton: CRC Press, 1978, pp. 165–173.
[41] E. Souteyrand, J. P. Cloarec, J. R. Martin, C. Wilson, I. Lawrence, S. Mikkelsen, and M. F. Lawrence, "Direct detection of the hybridization of synthetic homo-oligomer DNA sequences by field effect," *Journal of Physical Chemistry B*, vol. 101, pp. 2980–2985, 1997.
[42] X. Duan, Y. Li, N. K. Rajan, D. A. Routenberg, Y. Modis, and M. A. Reed, "Quantification of the affinities and kinetics of protein interactions using silicon nanowire biosensors," *Nature Nanotechnology*, vol. 7, pp. 401–7, 2012.
[43] Y. Cui, Q. Wei, H. Park, and C. M. Lieber, "Nanowire nanosensors for highly sensitive and selective detection of biological and chemical species," *Science*, vol. 293, pp. 1289–92, 2001.
[44] P. R. Nair, and M. A. Alam, "Design considerations of silicon nanowire biosensors," *IEEE Transactions on Electron Devices*, vol. 54, pp. 3400–3408, 2007.
[45] T. M. Squires, R. J. Messinger, and S. R. Manalis, "Making it stick: convection, reaction and diffusion in surface-based biosensors," *Nature Biotechnology*, vol. 26, pp. 417–26, 2008.
[46] E. Stern, J. F. Klemic, D. A. Routenberg, P. N. Wyrembak, D. B. Turner-Evans, A. D. Hamilton, D. A. Lavan, T. M. Fahmy, and M. A. Reed, "Label-free immunodetection with CMOS-compatible semiconducting nanowire," *Nature*, vol. 445, pp. 519–522, 2007.
[47] G. Zheng, F. Patolsky, Y. Cui, W. U. Wang, and C. M. Lieber, "Multiplexed electrical detection of cancer markers with nanowire sensor arrays," *Nature Biotechnology*, vol. 23, pp. 1294–301, 2005.
[48] A. Gao, N. Lu, Y. Wang, P. Dai, T. Li, X. Gao, Y. Wang, and C. Fan, "Enhanced sensing of nucleic acids with silicon nanowire field effect transistor biosensors," *Nano Letters*, vol. 12, pp. 5262–8, 2012.
[49] R. Tian, S. Regonda, J. Gao, Y. Liu, and W. Hu, "Ultrasensitive protein detection using lithographically defined Si multi-nanowire field effect transistors," *Lab Chip*, vol. 11, pp. 1952–61, 2011.
[50] S. M. Sze, *Semiconductor Devices: Physics and Technology*, 2nd ed. John Wiley & Sons, Inc., 2001.
[51] B. G. Streetman and S. Banerjee, *Solid State Electronic Devices*, 5th ed. Upper Saddle River, New Jersey: Prentice Hall, Inc., 2000.
[52] Z. Zhang, "Integration of silicide nanowires as Schottky barrier source/drain in FinFETs," 2008.
[53] L. Bousse, "Single electrode potentials related to flat-band voltage measurements on EOS and MOS structures," *Journal of Chemical Physics*, vol. 76, pp. 5128–5133, 1982.
[54] R. E. G. van Hal, J. C. T. Eijkel, and P. Bergveld, "A general model to describe the electrostatic potential at electrolyte oxide interfaces," *Advances in Colloid and Interface Science*, vol. 69, pp. 31–62, 1996.

[55] V. S. Bagotsky, *Fundamentals of Electrochemistry*, 2nd ed. Hoboken, NJ: John Wiley & Sons, Inc., 2005.
[56] Y. L. Bunimovich, Y. S. Shin, W.-S. Yeo, M. Amori, G. Kwong, and J. R. Heath, "Quantitative real-time measurements of DNA hybridization with alkylated nonoxidized silicon nanowires in electrolyte solution," *Journal of the American Chemical Society*, vol. 128, pp. 16323–31, 2006.
[57] X. P. A. Gao, G. Zheng, and C. M. Lieber, "Subthreshold regime has the optimal sensitivity for nanowire FET biosensors," *Nano Letters*, vol. 10, pp. 547–52, 2010.
[58] S. Sorgenfrei, C. Chiu, R. L. Gonzalez, Y.-J. Yu, P. Kim, C. Nuckolls, and K. L. Shepard, "Label-free single-molecule detection of DNA-hybridization kinetics with a carbon nanotube field-effect transistor.," *Nature Nanotechnology*, vol. 6, pp. 126–32, 2011.
[59] S. Chen, L. Nyholm, N. Jokilaakso, A. E. Karlström, J. Linnros, U. Smith, and S.-L. Zhang, "Current instability for silicon nanowire field-effect sensors operating in electrolyte with platinum gate electrodes," *Electrochemical and Solid-State Letters*, vol. 14, pp. J34–J37, 2011.
[60] S. Chen and S.-L. Zhang, "Contacting versus insulated gate electrode for Si nanoribbon field-effect sensors operating in electrolyte," *Analytical Chemistry*, vol. 83, pp. 9546–51, 2011.
[61] A. J. Bard and L. R. Faulkner, *Electrochemical Methods, Fundamentals and Applications*, 2nd ed. New York: John Wiley & Sons, Inc., 2001.
[62] T. Strachan and A. Read, *Human Molecular Genetics*, 4th ed. New York: Garland Science, 2010.
[63] "Isoelectric point." [Online]. Available: http://en.wikipedia.org/wiki/Isoelectric_point. [Accessed: 21-Nov-2012].
[64] P. A. E. Piunno, J. Watterson, C. C. Wust, and U. J. Krull, "Considerations for the quantitative transduction of hybridization of immobilized DNA," *Analytica Chimica Acta*, vol. 400, pp. 73–89, 1999.
[65] B. M. Venkatesan and R. Bashir, "Nanopore sensors for nucleic acid analysis," *Nature Nanotechnology*, vol. 6, pp. 615–24, 2011.
[66] P.-A. Nygren, "Alternative binding proteins: affibody binding proteins developed from a small three-helix bundle scaffold," *The FEBS Journal*, vol. 275, pp. 2668–76, 2008.
[67] "Affibody technology." [Online]. Available: http://www.abcam.com/index.html?pageconfig=resource&rid=10582&pid=10000&source=pagetrap. [Accessed: 20-Sep-2012].

[68] R. Pethig and D. B. Kell, “The passive electrical properties of biological systems: their significance in physiology, biophysics and biotechnology.,” *Physics in Medicine and Biology*, vol. 32, pp. 933–70, 1987.

[69] S. Chen, Z.-B. Zhang, L. Ma, P. Ahlberg, X. Gao, Z. Qiu, D. Wu, W. Ren, H.-M. Cheng, and S.-L. Zhang, “A graphene field-effect capacitor sensor in electrolyte,” *Applied Physics Letters*, vol. 101, p. 154106, 2012.

[70] Y.-B. Wang, Y. Assefaw-Redda, M. Gabig-Ciminska, S.-O. Enfors, M. Östling, and S.-L. Zhang, “A novel dual mode capacitor biosensor for real-time , label-free DNA detection,” *International Electron Device Meeting (IEDM)*, pp. 6–9, 2006.

[71] A. Qureshi, Y. Gurbuz, S. Kallempudi, and J. H. Niazi, “Label-free RNA aptamer-based capacitive biosensor for the detection of C-reactive protein,” *Physical Chemistry Chemical physics*, vol. 12, pp. 9176–82, 2010.

[72] M. Hedström, I. Y. Galaev, and B. Mattiasson, “Continuous measurements of a binding reaction using a capacitive biosensor,” *Biosensors and Bioelectronics*, vol. 21, no. 1, pp. 41–8, 2005.

[73] J. Xia, F. Chen, J. Li, and N. Tao, “Measurement of the quantum capacitance of graphene,” *Nature Nanotechnology*, vol. 4, pp. 505–9, 2009.

[74] W. Yang, K. R. Ratinac, S. P. Ringer, P. Thordarson, J. J. Gooding, and F. Braet, “Carbon nanomaterials in biosensors: should you use nanotubes or graphene?,” *Angewandte Chemie (International Ed. in English)*, vol. 49, pp. 2114–38, 2010.

[75] D. Du, Y. Yang, and Y. Lin, “Graphene-based materials for biosensing and bioimaging,” *MRS Bulletin*, vol. 37, pp. 1290–1296, 2012.

[76] D. Hisamoto, W. Lee, J. Kedzierski, H. Takeuchi, K. Asano, C. Kuo, E. Anderson, T. King, J. Bokor, and C. Hu, “FinFET — a self-aligned double-gate MOSFET scalable to 20 nm,” *IEEE Transactions on Electron Devices*, vol. 47, pp. 2320–2325, 2000.

[77] B. R. B., W. Stewart, and E. Lightfoot, *Transport Phenomena*, 2nd ed. New York: John Wiley & Sons, Inc., 2002.

[78] L. G. Leal, *Advanced Transport Phenomena: Fluid Mechanics and Convective Transport Processes*. Cambridge: Cambridge University Press, 2007.

[79] W. M. Deen, *Analysis of Transport Phenomena*. New York: Oxford University Press, 1998.

[80] M. Curreli, R. Zhang, F. N. Ishikawa, H.-K. Chang, R. J. Cote, C. Zhou, and M. E. Thompson, “Real-time, label-free detection of biological entities using nanowire-based FETs,” *IEEE Transactions on Nanotechnology*, vol. 7, pp. 651–667, 2008.

[81] E. Stern, A. Vacic, and M. A. Reed, “Semiconducting nanowire field-effect transistor biomolecular sensors,” *IEEE Transactions on Electron Devices*, vol. 55, pp. 3119–3130, 2008.
[82] R. S. Wagner and W. C. Ellis, “Vapor-Liquid-Solid mechanism of single crystal growth,” *Applied Physics Letters*, vol. 4, pp. 89–90, 1964.
[83] W. Lu and C. M. Lieber, “Semiconductor nanowires,” *Journal of Physics D: Applied Physics*, vol. 39, pp. R387–R406, 2006.
[84] B. X. Duan and C. M. Lieber, “General synthesis of compound semiconductor nanowires,” *Advanced Materials*, vol. 12, pp. 298–302, 2000.
[85] Y. Wu, Y. Cui, L. Huynh, C. J. Barrelet, D. C. Bell, and C. M. Lieber, “Controlled growth and structures of molecular-scale silicon nanowires,” *Nano Letters*, vol. 4, pp. 433–436, 2004.
[86] F. Patolsky, G. Zheng, and C. M. Lieber, “Fabrication of silicon nanowire devices for ultrasensitive, label-free, real-time detection of biological and chemical species,” *Nature Protocols*, vol. 1, pp. 1711–24, 2006.
[87] Y. Choi, T. King, and C. Hu, “A spacer patterning technology for nanoscale CMOS,” *IEEE Transactions on Electron Devices*, vol. 49, pp. 436–441, 2002.
[88] O. H. Elibol, D. Morisette, D. Akin, J. P. Denton, and R. Bashir, “Integrated nanoscale silicon sensors using top-down fabrication,” *Applied Physics Letters*, vol. 83, pp. 4613–4615, 2003.
[89] Y.-K. Choi, J. S. Lee, J. Zhu, G. A. Somorjai, L. P. Lee, and J. Bokor, “Sublithographic nanofabrication technology for nanocatalysts and DNA chips,” *Journal of Vacuum Science & Technology B*, vol. 21, pp. 2951–2955, 2003.
[90] N. A. Melosh, A. Boukai, F. Diana, B. Gerardot, A. Badolato, P. M. Petroff, and J. R. Heath, “Ultrahigh-density nanowire lattices and circuits,” *Science*, vol. 300, pp. 112–5, 2003.
[91] D. Wang, B. A. Sheriff, and J. R. Heath, “Silicon p-FETs from ultrahigh density nanowire arrays,” *Nano Letters*, vol. 6, pp. 1096–100, 2006.
[92] A. Kim, C. S. Ah, H. Y. Yu, J.-H. Yang, I.-B. Baek, C.-G. Ahn, C. W. Park, M. S. Jun, and S. Lee, “Ultrasensitive, label-free, and real-time immunodetection using silicon field-effect transistors,” *Applied Physics Letters*, vol. 91, p. 103901, 2007.
[93] N. Elfström, R. Juhasz, I. Sychugov, T. Engfeldt, A. E. Karlström, and J. Linnros, “Surface charge sensitivity of silicon nanowires: size dependence,” *Nano Letters*, vol. 7, pp. 2608–12, 2007.

[94] K. B. Sundaram, A. Vijayakumar, and G. Subramanian, “Smooth etching of silicon using TMAH and isopropyl alcohol for MEMS applications,” *Microelectronic Engineering*, vol. 77, pp. 230–241, 2005.
[95] Z. Zhang, S.-L. Zhang, M. Östling, and J. Lu, “Robust, scalable self-aligned platinum silicide process,” *Applied Physics Letters*, vol. 88, p. 142114, 2006.
[96] Z. Li, Y. Chen, X. Li, T. I. Kamins, K. Nauka, and R. S. Williams, “Sequence-specific label-free DNA sensors based on silicon nanowires,” *Nano Letters*, vol. 4, pp. 245–247, 2004.
[97] A. V. Anilkumar, C. P. Lee, and T. G. Wang, “Surface-tension-induced mixing following coalescence of initially stationary drops,” *Physics of Fluids A: Fluid Dynamics*, vol. 3, pp. 2587–2591, 1991.
[98] N. Jokilaakso, “Chemical modification of chips for ssDNA measurements.” 2009.
[99] F. Zhang, K. Sautter, A. M. Larsen, D. A. Findley, R. C. Davis, H. Samha, and M. R. Linford, “Chemical vapor deposition of three aminosilanes on silicon dioxide: surface characterization, stability, effects of silane concentration, and cyanine dye adsorption,” *Langmuir*, vol. 26, pp. 14648–54, 2010.
[100] T. P. Sullivan and W. T. S. Huck, “Reactions on monolayers: organic synthesis in two dimensions,” *European Journal of Organic Chemistry*, vol. 2003, pp. 17–29, 2003.
[101] S. Flink, F. C. J. M. van Veggel, and D. N. Reinhoudt, “Sensor functionalities in self-assembled monolayers,” *Advanced Materials*, vol. 12, pp. 1315–1328, 2000.
[102] E. T. Vandenberg, L. Bertilsson, B. Liedberg, K. Uvdal, R. Erlandsson, H. Elwing, and I. Lundström, “Structure of 3-aminopropyl triethoxy silane on silicon oxide,” *Journal of Colloid and Interface Science*, vol. 147, pp. 103–118, 1991.
[103] B. Dorvel, B. Reddy, I. Block, P. Mathias, S. E. Clare, B. Cunningham, D. E. Bergstrom, and R. Bashir, “Vapor-phase deposition of monofunctional alkoxysilanes for sub-nanometer-level biointerfacing on silicon oxide surfaces,” *Advanced Functional Materials*, vol. 20, pp. 87–95, 2010.
[104] I. Lee and R. P. Wool, “Controlling amine receptor group density on aluminum oxide surfaces by mixed silane self assembly,” *Thin Solid Films*, vol. 379, pp. 94–100, 2000.
[105] M. Bras, V. Dugas, F. Bessueille, J. P. Cloarec, J. R. Martin, M. Cabrera, J. P. Chauvet, E. Souteyrand, and M. Garrigues, “Optimisation of a silicon/silicon dioxide substrate for a fluorescence DNA microarray,” *Biosensors and Bioelectronics*, vol. 20, pp. 797–806, 2004.

[106] “Product information.” [Online]. Available: http://www.sigmaaldrich.com/etc/medialib/docs/Sigma/Product_Information_Sheet/2/i6634pis.Par.0001.File.tmp/i6634pis.pdf. [Accessed: 21-Nov-2012].
[107] J. Hahm and C. M. Lieber, “Direct ultrasensitive electrical detection of DNA and DNA sequence variations using nanowire nanosensors,” *Nano Letters*, vol. 4, pp. 51–54, 2004.
[108] E. Stern, A. Vacic, N. K. Rajan, J. M. Criscione, J. Park, B. R. Ilic, D. J. Mooney, M. A. Reed, and T. M. Fahmy, “Label-free biomarker detection from whole blood,” *Nature Nanotechnology*, vol. 5, pp. 138–42, 2010.
[109] N. Elfström, A. E. Karlström, and J. Linnros, “Silicon nanoribbons for electrical detection of biomolecules,” *Nano Letters*, vol. 8, pp. 945–949, 2008.
[110] S. Park, H. Boo, Y. Kim, J.-H. Han, H. C. Kim, and T. D. Chung, “*p*H-sensitive solid-state electrode based on electrodeposited nanoporous platinum,” *Analytical Chemistry*, vol. 77, pp. 7695–701, 2005.
[111] J. Noh, S. Park, H. Boo, H. C. Kim, and T. D. Chung, “Nanoporous platinum solid-state reference electrode with layer-by-layer polyelectrolyte junction for *p*H sensing chip,” *Lab Chip*, vol. 11, pp. 664–71, 2011.
[112] S. Chen and S.-L. Zhang, “Gate coupling and carrier distribution in silicon nanowire/nanoribbon transistors operated in electrolyte,” *Journal of Vacuum Science & Technology A*, vol. 29, p. 011022, 2011.
[113] L. Bousse and P. Bergveld, “The role of buried OH sites in the response mechanism of inorganic-gate *p*H-sensitive ISFETs,” *Sensors and Actuators*, vol. 6, pp. 65–78, 1984.
[114] S. Jamasb, S. Collins, and R. L. Smith, “A physical model for drift in *p*H ISFETs,” *Sensors and Actuators B: Chemical*, vol. 49, pp. 146–155, 1998.
[115] S. Jamasb, S. D. Collins, and R. L. Smith, “A physical model for threshold voltage instability in Si_3N_4-gate H^+-sensitive FET’s (*p*H ISFET's),” *IEEE Transactions on Electron Devices*, vol. 45, pp. 1239–1245, 1998.
[116] “International Technology Roadmap for Semiconductors.” [Online]. Available: http://www.itrs.net/.

Acta Universitatis Upsaliensis

Digital Comprehensive Summaries of Uppsala Dissertations from the Faculty of Science and Technology 1018

Editor: The Dean of the Faculty of Science and Technology

A doctoral dissertation from the Faculty of Science and Technology, Uppsala University, is usually a summary of a number of papers. A few copies of the complete dissertation are kept at major Swedish research libraries, while the summary alone is distributed internationally through the series Digital Comprehensive Summaries of Uppsala Dissertations from the Faculty of Science and Technology.

Distribution: publications.uu.se
urn:nbn:se:uu:diva-194015

ACTA
UNIVERSITATIS
UPSALIENSIS
UPPSALA
2013